Materials & Design 267 (2026) 116414

Contents lists available at ScienceDirect

Materials & Design

journal homepage: www.elsevier.com/locate/matdes

Process-dependent phase evolution in thermally sprayed $Li_4Ti_5O_{12}$ thin-film anodes revealed by synchrotron and surface analysis

Arman Hasani [a,*], Antti Salminen [a], Shrikant Joshi [b], Malgorzata Grazyna Makowska [c], Behnam Chameh [d], Vesa-Pekka Lehto [d], Vinay Gidla [a], Sneha Goel [e], Ilari Angervo [f], Ashish Ganvir [a]

[a] Digital Manufacturing and Surface Engineering (DMS) Research Group, Department of Mechanical and Materials Engineering, Faculty of Technology, University of Turku, Finland
[b] Department of Engineering Science, University West, Sweden
[c] Paul Scherrer Institute, Laboratory for Synchrotron Radiation and Femtochemistry and Laboratory for Nuclear Materials, Advanced Nuclear Materials Group, Switzerland
[d] Department of Technical Physics, University of Eastern Finland, Kuopio, Finland
[e] Advanced Materials for Nuclear Energy, VTT Technical Research Centre of Finland, Finland
[f] Wihuri Physical Laboratory, Department of Physics and Astronomy, University of Turku, Finland

ARTICLE INFO

Keywords:
Atmospheric plasma spraying
Suspension Plasma Spraying
High Velocity Oxy Fuel spraying
$Li_4Ti_5O_{12}$ (LTO)
Synchrotron μXRD and μXRF
Process–structure–property correlation

ABSTRACT

Understanding process-induced phase evolution in thermally sprayed $Li_4Ti_5O_{12}$ (LTO) thin-films is critical for developing scalable battery electrodes with stable electrochemical performance. This study comparatively investigates Atmospheric Plasma Spraying (APS), Suspension Plasma Spraying (SPS), and High-Velocity Oxy-Fuel (HVOF) processing of LTO thin-film anodes using SEM/EDS, laboratory XRD, synchrotron μXRD/μXRF mapping, XPS, and electrochemical characterization. Synchrotron μXRD revealed distinct process-dependent phase evolution governed by thermal exposure and quenching behavior. HVOF retained the highest spinel LTO fraction (66.8 %), APS retained 65.1 %, while SPS showed the strongest decomposition with only 53.5 % LTO together with increased Li_2TiO_3 (43.5 %) and TiO_2 formation (3.0 %). XPS analysis identified Li_2CO_3 surface formation in APS and HVOF coatings, whereas SPS exhibited strong surface lithium depletion. Electrochemical measurements showed that APS-LTO exhibited the most favorable electrochemical response, with a working voltage of ~1.56 V vs. Li/Li^+ and lower polarization resistance (~18.7 kΩ) compared with SPS and HVOF coatings. The results establish process–structure–property relationships linking thermal spray conditions with lithium retention, phase stability, and electrochemical behavior in thermally sprayed LTO thin-films.

1. Introduction

The ever-increasing demand for efficient and reliable energy-storage systems has driven the search for electrode materials that combine high stability, safety, and rate capability [1]. Among various candidates, lithium titanate ($Li_4Ti_5O_{12}$, LTO) has emerged as a benchmark anode material owing to its "zero-strain" spinel structure, flat operating voltage (~1.55 V vs. Li^+/Li), and exceptional cycling stability [2,3,4]. These characteristics make LTO suitable not only for high-power lithium-ion batteries but also for emerging thin-film solid-state energy-storage systems where interfacial and thermal stability are critical [2,5,6].

Beyond its zero-strain signature, LTO's practical performance is constrained by low electronic conductivity and moderate Li^+ diffusivity, motivating efforts to tailor its microstructure and surface chemistry in thin films [7,8]. Strategies such as cation doping, conductive additives, and surface carbonate management emphasize that phase purity and surface lithium states are decisive for rate and cycling behavior [9,10,11]. Thermal-spray-derived thin-film LTO provides a distinct pathway that can control phase constitution and surface Li retention in situ through the adjustment of deposition temperature and quenching dynamics [12 13].

Although the intrinsic electrochemical properties of LTO are well established [14], translating its performance into scalable thin-film

* Corresponding author.
E-mail address: arman.hasani@utu.fi (A. Hasani).

https://doi.org/10.1016/j.matdes.2026.116414
Received 17 December 2025; Received in revised form 19 May 2026; Accepted 15 June 2026
Available online 16 June 2026

electrodes remains challenging. Conventional fabrication routes such as slurry casting, tape casting, or sputtering yield high structural precision but suffer from low throughput, high cost, and limited thickness scalability [15,16,17]. In contrast, thermal spray techniques offer unique advantages for fabricating dense or porous ceramic thin and thick films over large areas with industrially viable deposition rates[1819,20]. Methods such as Atmospheric Plasma Spraying (APS), Suspension Plasma Spraying (SPS), and High-Velocity Oxy-Fuel (HVOF) have therefore gained attention as alternative routes for producing functional oxide films, including electrode and electrolyte layers for energy storage applications [12,21,22,23].

Process physics differs fundamentally across these techniques by virtue of the fact that key governing factors such as gas enthalpy, droplet or particle residence time, cooling rate etc. vary substantially [24,25]. APS/SPS expose feedstock to extremely high thermal fluxes, while HVOF operates at lower particle temperatures but imparts high kinetic energy and rapid quenching [18,26,27]. In LTO, these variations control competing thermodynamic and kinetic pathways such as the decomposition reaction (at 840 °C)

$$(Li_4Ti_5O_{12} \rightarrow 2\ Li_2TiO_3 + 3\ TiO_2)\ [28] \quad (1)$$

and also govern lithium volatilization via LiOH(g) formation in humid plasma environments (notably SPS) followed by Li_2CO_3 re-precipitation upon cooling [29,30]. Understanding how these thermal and chemical environments dictate phase stability and lithium retention is essential for achieving controlled fabrication of LTO thin-films with preserved spinel integrity[12].

Conventional characterization techniques such as SEM/EDS, XRD, profilometry, and electrochemical testing provide valuable morphological and averaged structural information but fail to capture localized phase and chemical heterogeneity, particularly near interfaces but also within the bulk thin-film. On the contrary, synchrotron-based micro-X-ray diffraction (μXRD) and micro-X-ray fluorescence (μXRF) enable mapping of crystalline phases and elemental distributions with micron-scale precision through thickness within the thin-film [31,32,33]. When combined with X-ray photoelectron spectroscopy (XPS), these methods provide a multi-scale picture linking bulk phase investigation and surface lithium chemistry, thereby revealing mechanisms of thermal-spray-induced transformations [12,21,22,34].

Despite the growing interest in thermal-sprayed LTO [13,23,35], a comparative, mechanism-centric study that links the process physics of APS, SPS, and HVOF to phase-evolution pathways and surface lithium states through advanced multi-scale characterization has not yet been reported. Despite growing interest in thermally sprayed $Li_4Ti_5O_{12}$ (LTO), prior studies have focused on single processes and bulk characterization, leaving phase evolution in thin-films poorly understood. At the time this work was conceived, no studies had systematically investigated thermally sprayed LTO as a thin-film anode across multiple spray techniques. This study presents a comparative analysis of APS, SPS, and HVOF using identical feedstock, establishing a unified process–structure–property framework. A key novelty is the application of high-resolution synchrotron μXRD/μXRF mapping, for the first time enabling depth-resolved and spatially localized characterization of phase evolution, elemental distribution, and interface behavior in such thin-films. By integrating these results with XPS and electrochemical testing, the work reveals new mechanistic insights into lithium retention, volatilization, and process-dependent phase stability. These findings provide both fundamental understanding and practical guidelines for designing high-performance thermally sprayed thin-film electrodes. This study hypothesizes that process-specific thermal and chemical environments deterministically steer LTO phase evolution and surface lithium retention, and that these mechanisms can be resolved by combining synchrotron μXRD/μXRF with XPS and correlated with electrochemical performance. Accordingly, this work: (a) establishes a comparative framework across APS, SPS, and HVOF for LTO thin films; (b) quantifies phase evolution (LTO ↔ Li_2TiO_3 + TiO_2) using synchrotron μXRD and maps elemental distributions via μXRF; (c) resolves surface lithium chemistry (Li_2CO_3 formation and Li depletion) through XPS; and (d) correlates these findings with working voltage and cycling stability to derive generalized process–structure–property relationships for thermally sprayed LTO electrodes.

2. Materials and methods

2.1. Feedstock materials and substrates

Commercial $Li_4Ti_5O_{12}$ (LTO) powder from NEI Corporation (USA) with purity > 99.9 %, particle size distribution (d50) 1.5 μm to 3.0 μm was used as the base material. For the SPS process, the suspension was formulated in-house using the aforementioned commercially available powder. A suspension was prepared in deionized water containing 20 wt % LTO powder and 1 wt% 1-Methyl-2-pyrrolidinone (NMP) (Sigma-Aldrich) as an additive. The suspension was continuously stirred during spraying to prevent sedimentation. For the APS and HVOF processes, the same LTO chemistry was used but with a coarser sieved fraction (6–7 μm) provided by Toshima Manufacturing Co Ltd, Japan, to ensure consistent composition across all processes.

The substrates for APS and HVOF processes were commercially pure aluminum (Al) discs, and for SPS was Stainless steel-304, each measuring 25 mm in diameter and 2 mm in thickness. Prior to deposition, all substrates were grit blasted with a 125 μm alumina grit, and then cleaned. Table 1 presents the chemical composition of the LTO powder as determined by energy dispersive spectroscopy (EDS), while Fig. 1 illustrates the powder morphology and elemental distribution observed via scanning electron microscopy (SEM) and EDS.

2.2. Deposition processes

2.2.1. Suspension plasma spraying (SPS)

Axial III high-power plasma torch with NanoFeed 350 suspension feeder (Northwest Mettech Corp., Vancouver, Canada) was used. The process parameters used for depositing LTO suspension are listed in Table 2. Sequential spray passes were used to build up a ~ 70 μm thickness.

2.2.2. Atmospheric plasma spraying (APS)

A Mettech Axial III high-power plasma torch (Northwest Mettech Corp., Vancouver, Canada), paired with a G4™ Gravimetric Powder Feeder, was employed for the APS thin-film deposition. The spray parameters for depositing LTO powder via APS are given in Table 3. Sequential spray passes were used to build up a ~ 40 μm thickness.

2.2.3. High velocity oxy-fuel (HVOF)

HVOF spraying was performed using a DJ2700 gun (Oerlikon Metco) with propane as the fuel at the Thermal Spraying Engineering (TSE) facility in Malmö, Sweden. LTO powders (d_{50} = 6–7 μm) were deposited onto grit-blasted Al substrates. Sequential spray passes were used to build up a ~ 18 μm thickness. The HVOF experiments should therefore be interpreted as exploratory trials intended to evaluate the thermal exposure effects of the process on LTO powders rather than as a fully optimized coating process.

The coating conditions employed in the present study were selected based on prior process optimization studies and preliminary trials to

Table 1
Chemical composition of LTO powder measured by EDS.

Element	Li	Ti	O	Cl, Si, Al,
LTO powder (wt %)	(Excluding Li, which could not be detected)	54.4	45.2	0.4

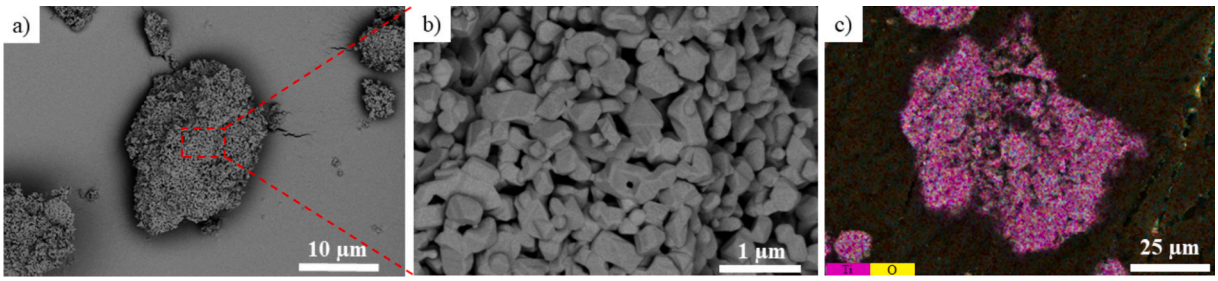

Fig. 1. SEM micrographs at (a) low and (b) high magnifications revealing the irregular morphology of LTO powder particles, and (c)EDS image of LTO powder.

Table 2
SPS parameters utilized for deposition of LTO suspension.

Nozzle size (inch)	Suspension Feed (mL/min)	Current (A)	Gas Composition (%)	Total Gas Flow (L/min)	Power (kW)	Enthalpy (kJ)	Stand-of-Distance (mm)	No. of Passes
5/16	42	220	50Ar-30 N_2-20H_2	200	110	11	70	20

Table 3
Spray parameters for APS deposition of LTO.

Nozzle size (inch)	Current (A)	Power (KW)	Enthalpy (kJ)	Gas Composition (%)	Gas flow rate (l/min)	Powder feed rate (g/min)	Stand-of-Distance (mm)	No. of Passes
5/16	150	73.2	6.7	80Ar-10 N_2-10H_2	280	30	130	4

obtain continuous and stable thin-film deposits with low porosity levels (<3 %). Detailed optimization procedures and microstructural analyses for these coatings have been reported in our previous work [23,36,37].

2.3. Characterization

2.3.1. SEM/EDS and surface topography

Scanning electron microscopy (SEM) was performed using an APREO field emission SEM (FE-SEM) system (Thermo Fisher Scientific, Waltham, MA, USA), equipped with an energy-dispersive X-ray spectroscopy (EDS) detector. SEM imaging was conducted at an acceleration voltage of 5 kV, while EDS analysis was carried out at 15 kV or 20 kV, depending on the sample requirements. Furthermore, surface topography and roughness were evaluated using the Alicona Infinite Focus G6 optical 3D measurement system (Bruker, Billerica, MA, USA), operated with MetMax software (version 3.0).

2.3.2. Lab-scale XRD and Rietveld analysis

Conventional lab-scale X-Ray Diffraction (XRD) analysis was carried out using a Philips X'Pert PRO MPD diffractometer (Malvern Panalytical, The Netherlands). Samples were mounted on a metal sample holder and scanned over a 2θ range of 10° to 90°. Measurements were conducted in θ/2θ Bragg–Brentano geometry using Cu Kα radiation (λ = 1.54 Å). A PIXcel1D detector (Panalytical, The Netherlands) was employed for data collection.

2.3.3. Focused ion beam (FIB) preparation

A focused ion beam (FIB) was employed to extract a sample from the LTO thin-film for microstructural analysis. The procedure utilized a Xe^+ ion beam operated at 30 kV for milling and 12 kV for carbon deposition, enabling the attachment of the manipulator to the microsample for lift-out and subsequent mounting on a pin for x-ray measurements, i.e., synchrotron µXRD/µXRF (see Fig. 2). A comprehensive explanation of this part can be found in our earlier work [12].

2.3.4. Synchrotron µXRD/µXRF

The chemical composition and crystalline phases in the sample were analyzed using µXRF and µXRD contrast microscopy at the microXAS beamline of the Swiss Light Source (PSI) [38], as illustrated schematically in Fig. 3, µXRD data were collected with a Dectris Eiger 4 M single-photon counting detector [39], while µXRF measurements utilized four SDD detectors positioned around the sample. During raster scanning of the ceramic cross-sections, µXRD and µXRF data were simultaneously acquired with the detector arrangement shown in Fig. 3. The X-ray beam was focused to 1 µm, and the sample was moved in 0.5 µm increments (in both x and y directions) perpendicular to the beam, with a 200 ms acquisition time per point. Further methodological details can be found in Colldeweih et al. [40]. The X-ray beam had a wavelength of λ = 0.6812 Å. Data collection covered an area of 250 × 200 µm with a resolution of 1 × 1 µm pixels and 0.5 µm scan steps. Azimuthal integration of the diffraction rings was performed using the pyFAI Python

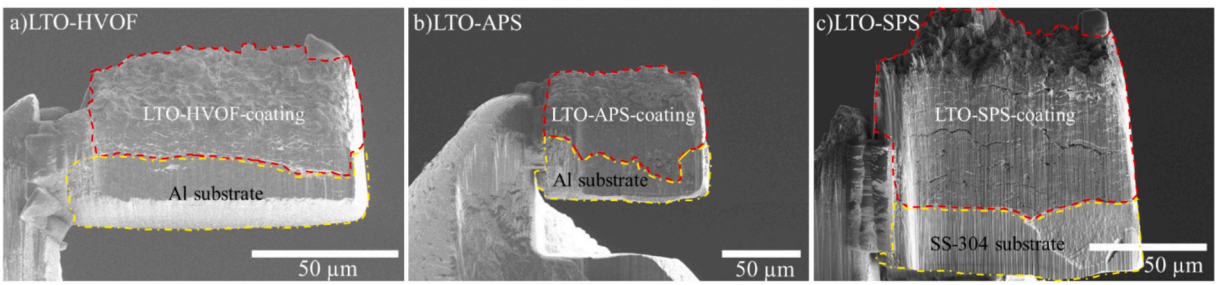

Fig. 2. SEM images of FIB milled samples, a)LTO-HVOF, b)LTO-APS, c)LTO-SPS.

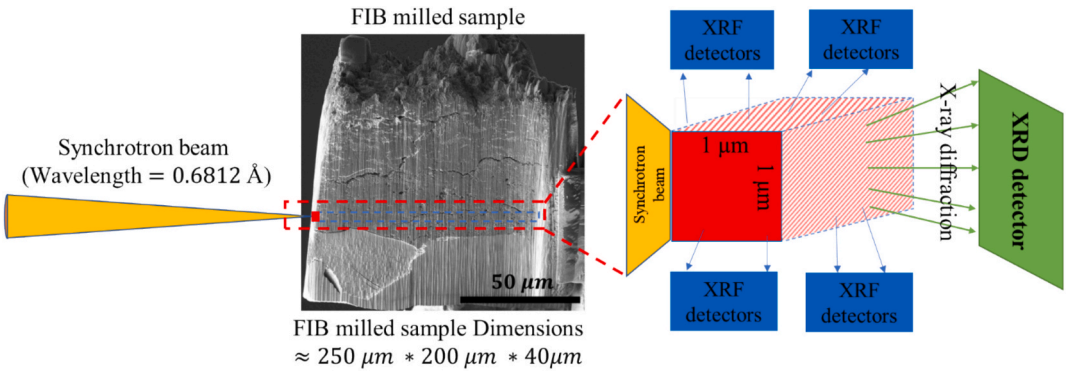

Fig. 3. Schematic illustration of the synchrotron μXRD and μXRF measurements[12].

library [41], assigning each integrated diffraction pattern to a pixel in the scanned region, producing 3000 XRD intensity maps at specific diffraction angles. Concurrently, μXRF spectra were acquired for each pixel and processed using the PyMca software [42], generating spatial maps of elemental distributions. Together, the μXRD and μXRF data provided complementary insights into the structural and compositional features of the sample. Phase identification and XRD data analysis were performed using X'Pert HighScore Plus software (version 4.9). By applying specific adjustments in the X'Pert HighScore Plus software, particularly converting the wavelength to $\lambda = 0.68123$ Å, the synchrotron μXRD data were successfully analyzed using the same software. Furthermore, the phase fractions shown in the pie charts were quantitatively determined by Rietveld refinement of the XRD patterns (both μXRD and Lab-scale XRD) obtained from the selected regions.

2.3.5. X-ray photoelectron spectroscopy (XPS)

X-ray photoelectron spectroscopy (XPS) was carried out on all the thin-films generated by the three processes using a ThermoFisher Nexsa (ESCA) system. For the survey scans, a step size of 1 eV was applied across binding energies from 0 to 1350 eV, while a finer step size of 0.1 eV was used for core element scans. Data obtained from XPS were processed using Avantage software. The charge correction was applied by taking the C-C as the reference. For the XPS analysis, the background correction was subtracted using the smart background function (improved Shirley-type background) while peaks are fitted using a Gaussian-Lorentzian distribution.

2.4. Electrochemical testing

For electrochemical characterization, all samples were laser-cut, with a diameter of 0.8 mm, the thickness of LTO-APS, SPS, And HVOF electrodes were 40, 70, and 18, respectively. Then the samples were dried in a vacuum oven at 100 °C for 24 h before cell assembly. The mass loading of the coated active materials was controlled between 6–7 mg/cm2. The ECC-Combi (From EL-Cell) was used for assembly in a glovebox under an Ar atmosphere with Li foil as the counter electrode, 140 μL of 1 M LiPF6 in ethylene carbonate and dimethyl carbonate (v/v 50/50) (battery grade, Sigma-Aldrich) as the liquid electrolyte, and Whatman GF/A glass microfiber filter as the separator. The cyclic voltammetry (CV), rate, and cycling tests were performed between 1.0 V and 2.5 V. For the rate and cycling tests, the initial cycle was performed at 0.05C, followed by 10 cycles each at 0.1C, 0.2C, 0.5 C, 1C, and 2C, and followed by 150 cycles at 0.5 C. The C-rate was based on the theoretical capacity of LTO (175 mA.g-1). The current density values used in testing LTO anodes correspond with the C-rate current density (1C = 1.05 mAh). EIS measurements were conducted with an AC amplitude of 5 mV over a frequency range of 10 kHz to 10 mHz after 30 min rest. All electrochemical tests were performed on a Biologic BCS-805cycler at room temperature (22 °C).

3. Results

3.1. Surface morphology and roughness

Fig. 4 illustrates the top-surface morphology and quantitative roughness values of the $Li_4Ti_5O_{12}$ (LTO) thin-films produced by APS, HVOF, and SPS. APS produced the roughest thin-film surface (Sa ≈ 11.79 μm), followed by HVOF (Sa ≈ 9.15 μm), while SPS yielded the smoothest thin-film surface (Sa ≈ 7.84 μm). The observed differences reflect the contrasting feedstock states, particle velocities, and thermal histories associated with each thermal spray process.

The APS thin-film exhibits a relatively coarse and irregular surface morphology with pronounced surface asperities and heterogeneous topographical features, characteristic of high-enthalpy powder-based plasma spraying [43]. The HVOF thin-film displays comparatively smoother splat-like surface features with intermediate roughness values (Sa ≈ 9.15 μm), which may be associated with the combined effects of moderate flame temperature and high particle velocity during deposition [44].

The SPS thin-film exhibits the smoothest top-surface morphology among the three coatings. The use of suspension feedstock containing -finer LTO particles promotes improved droplet spreading and formation of finer surface features during deposition, resulting in reduced surface roughness [45,46]. Previous studies have similarly reported lower roughness and more uniform top-surface morphology in SPS-derived ceramic coatings owing to the finer feedstock characteristics and droplet-based deposition mechanism [21]. However, suspension trajectory, atomization behavior, and plasma conditions can strongly influence the final surface morphology and roughness evolution in SPS coatings [47].

Overall, the surface roughness hierarchy (SPS < HVOF < APS) reflects the balance between particle/droplet melting, kinetic energy, and quenching behavior inherent to each deposition process [48,49,50]. Such top-surface morphological variations can influence electrode/electrolyte interfacial contact and consequently affect electrochemical response in ceramic battery electrodes [44].

It should also be noted that the measured roughness values may additionally be influenced by the initial substrate topography resulting from grit blasting using 125 μm alumina particles prior to deposition. Since the APS and HVOF coatings are relatively thin (~40 μm and ~ 18 μm, respectively), partial inheritance of the substrate waviness and anchor profile may contribute to the comparatively higher measured roughness values. In contrast, the thicker SPS coating (~70 μm) may partially mask the underlying substrate topography.

3.2. Phase composition and structural evolution

3.2.1. Synchrotron μXRD phase analysis

The detection and spatial quantification of thermally sprayed LTO

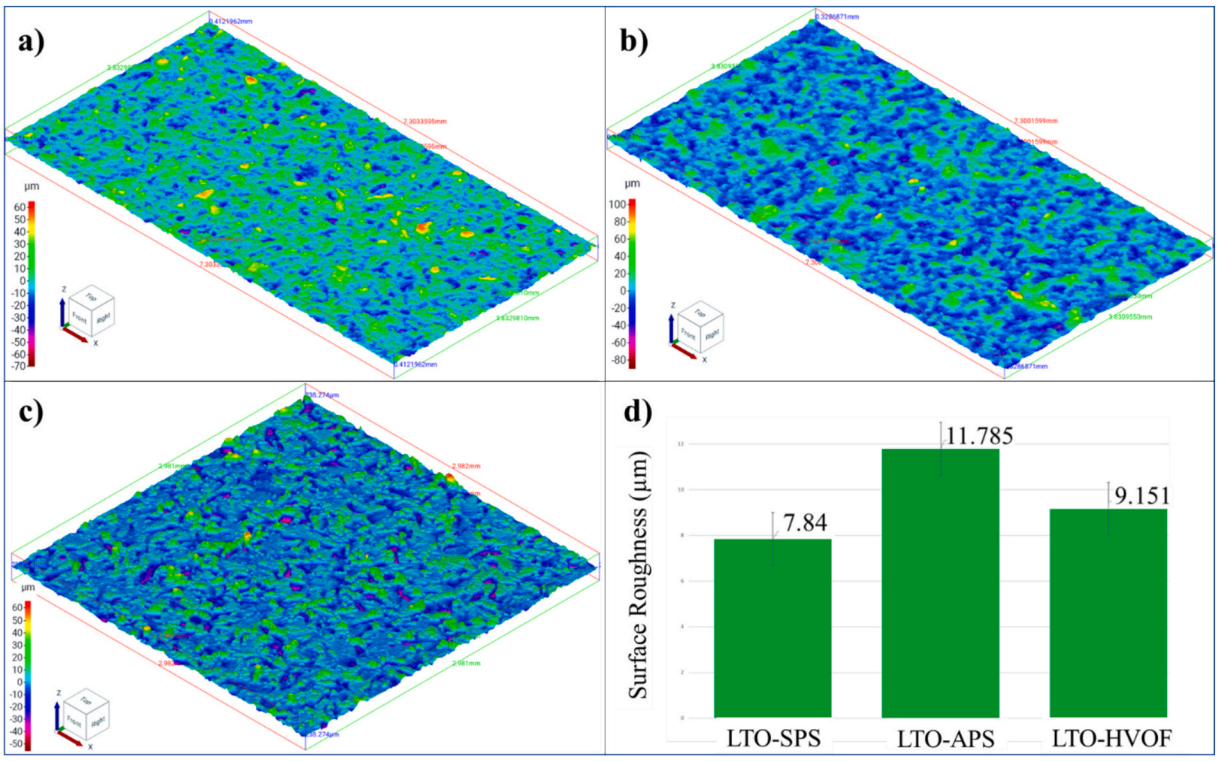

Fig. 4. Surface morphology and surface roughness of thermally sprayed LTO thin-films: (a) HVOF, (b) APS, (c) SPS, and (d) quantitative roughness comparison. SPS exhibits the smoothest surface (Sa ≈ 7.84 μm), followed by HVOF (9.151 μm) and APS (11.785 μm). The trend reflects differences in feedstock form, particle heating, and quenching rate inherent to each process [48,49,50].

phases were obtained by synchrotron-based μXRD, which unlike conventional lab-scale XRD that provides bulk-averaged information over a large gauge volume offers micron-scale resolution and enables non-destructive, depth-resolved phase identification across the full thin-film thickness. This capability is particularly important for thermally sprayed thin-films, where phase composition may vary with through-thickness thermal gradients and splat-by-splat morphology.

This approach confirms that thermal decomposition of LTO is a critical concern in high-temperature spray processes. LTO is valued for its "zero-strain" behavior during (de)lithiation and high structural stability in cycling, with a theoretical capacity of ~ 175 mAh g^{-1} [51]. However, it becomes thermally unstable above ~ 800–900 °C, particularly under oxidizing conditions or extended thermal exposure, promoting transformation to Li_2TiO_3 and TiO_2 [52]. In plasma-based deposition (APS/SPS), lithium depletion by volatilization or diffusion accelerates this transformation (Fig. 5), which follows Equation 1.

The extent of decomposition depends on thermal load, exposure time, and quench rate. In SPS, extreme plasma conditions and plasma–liquid interactions (droplet atomization, rapid solvent flash-off) intensify Li depletion and favor Li_2TiO_3/TiO_2 formation [12]. In contrast, HVOF offers lower effective particle temperatures, short residence times, and faster cooling rate which leads to better preserve of the spinel phase; APS experiences high thermal input but lacks the liquid-phase chemistry of SPS, leading to similar LTO preservation to HVOF within the μXRD-mapped regions (see figure 5).

Quantitative Rietveld analysis of the μXRD data (Fig. 5) shows this trend explicitly: HVOF retains 66.8 % LTO with 32.8 % Li_2TiO_3 and 0.4 % TiO_2; APS retains 65.1 % LTO with 34.0 % Li_2TiO_3 (TiO_2 below detection in the mapped ROI); SPS contains ~ 53.5 % LTO, ~43.5 % Li_2TiO_3, and ~ 3.0 % TiO_2. Thus, APS ≈ HVOF in LTO retention, whereas SPS shows the lowest LTO and the highest TiO_2 fraction among the three.

Regarding the decomposition products, Li_2TiO_3 (monoclinic) comprises alternating Li and TiO_6 octahedral layers and is thermally stable up to ~ 1200 °C and chemically inert in many environments [53]. Despite these structural merits, its electrochemical properties are inferior to LTO: lower electronic/ionic transport leads to practical capacities < 50 mAh.g^{-1}, with redox mainly from the Ti^{4+}/Ti^{3+} couple over ~ 1.5–3.0 V vs. Li^+/Li. Consequently, Li_2TiO_3 is more often used as a passive/functional layer (e.g., buffer/SEI-like interlayers in solid-state systems) rather than as an active anode, whereas its presence within an LTO anode typically reduces capacity and increases impedance [29].

In summary, the formation of Li_2TiO_3 within LTO thin-films is a clear indicator of process-induced degradation. Consistent with μXRD phase quantification, SPS exhibits elevated Li_2TiO_3 (43.5 %) and TiO_2 (3.0 %), while APS and HVOF retain > 65.0 % LTO with only ~ 34 % Li_2TiO_3 and negligible TiO_2. These observations align with prior reports linking plasma thermal exposure to phase instability and lithium depletion in LTO [12,13,54,55]. Practically, the sensitivity of LTO and the electrochemical inferiority of Li_2TiO_3 underscore the need to tailor spray parameters to minimize decomposition and preserve spinel-rich microstructures for optimal anode performance.

3.2.2. *Synchrotron μXRF elemental mapping*

Complementary to the μXRD results, synchrotron-based μXRF analysis was employed to evaluate the spatial distribution of elements and interface integrity in the thermally sprayed LTO thin-films (Fig. 6). The μXRF technique provides high-sensitivity elemental mapping with micron-scale resolution and, when correlated with μXRD, offers a direct visualization of local chemical homogeneity across the thin-film cross-section [56].

The Ti-K_α emission maps exhibit a continuous and uniform distribution throughout all three thin-films, indicating dense, well-bonded microstructures without significant voids or delamination. The uniform Ti signal in the HVOF and APS thin-films further confirms homogeneous splat stacking and limited phase segregation across the thickness.

It should be noted that Li cannot be directly detected by μXRF

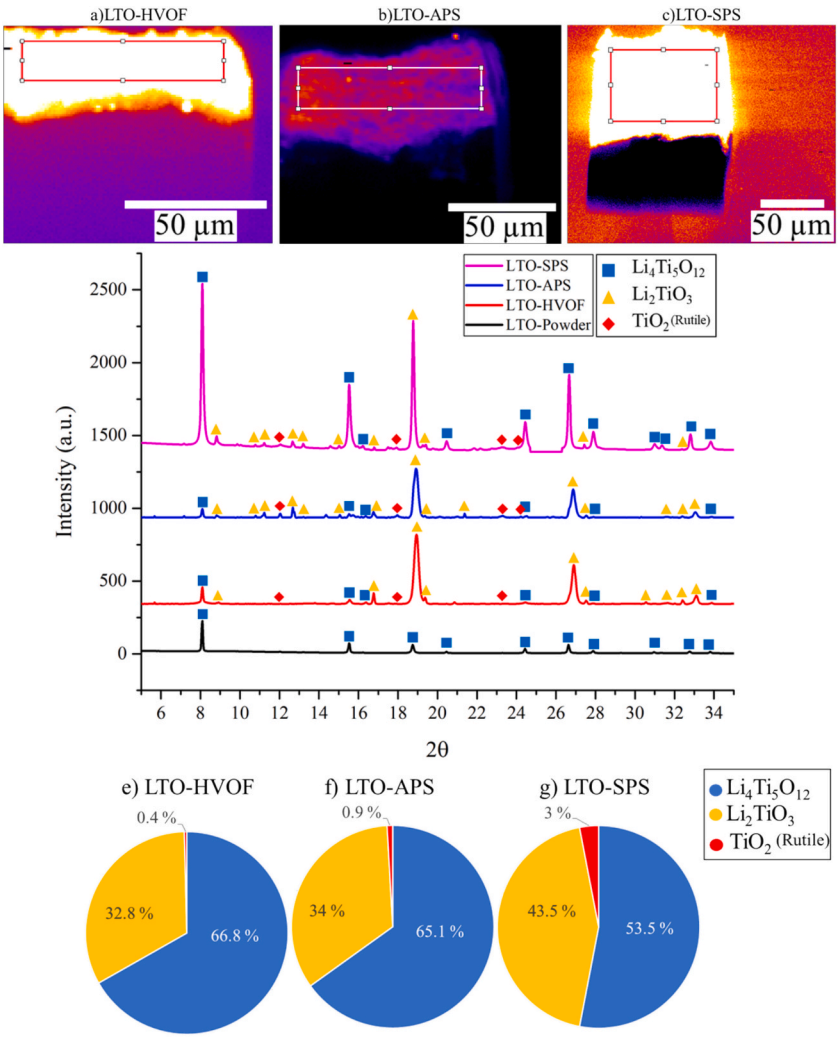

Fig. 5. Synchrotron µXRD analysis of thermally sprayed LTO thin-films: (a–c) mapped Region of Interests (ROIs); (d) representative integrated patterns; (e–g) Rietveld-derived phase fractions. APS and HVOF retain similar LTO levels (65.1 % and 66.8 %, respectively), while SPS shows reduced LTO (53.5 %) with higher Li_2TiO_3 (43.5 %) and TiO_2 (3 %). Differences reflect nominal process enthalpy and, for SPS, plasma–liquid effects.

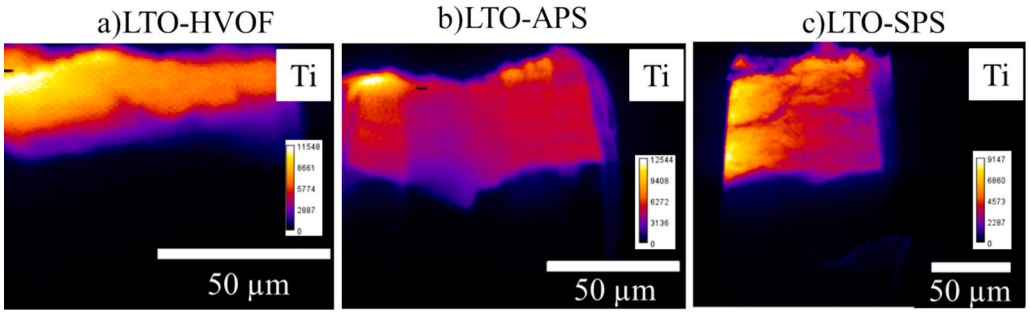

Fig. 6. Synchrotron µXRF elemental maps of FIB-milled cross-sections for thermally sprayed LTO thin-films: (a) HVOF, (b) APS, and (c) SPS. Li is not detectable by µXRF and is assessed indirectly via XPS and phase analysis.

because of its low atomic number [57]. Therefore, the Li distribution is inferred indirectly from the relative Ti and O intensities and from complementary XPS results (Section 3.4). Combined µXRD–µXRF mapping confirms that all thin-films are well bonded to their substrates, with APS and HVOF displaying uniform phase and elemental profiles, while SPS shows localized gradients consistent with its higher nominal plasma enthalpy and droplet-based deposition mechanism.

3.2.3. *Laboratory XRD analysis*

Conventional laboratory XRD measurements were conducted to obtain a bulk-averaged assessment of the crystalline phases in the thermally sprayed LTO thin-films (Fig. 7). Unlike the high spatial resolution of synchrotron µXRD, lab XRD provides a broader overview with good statistics, integrating diffraction from a much larger gauge volume and thereby complementing the localized µXRD results [58].

The diffraction patterns of all thin-films confirm the coexistence of

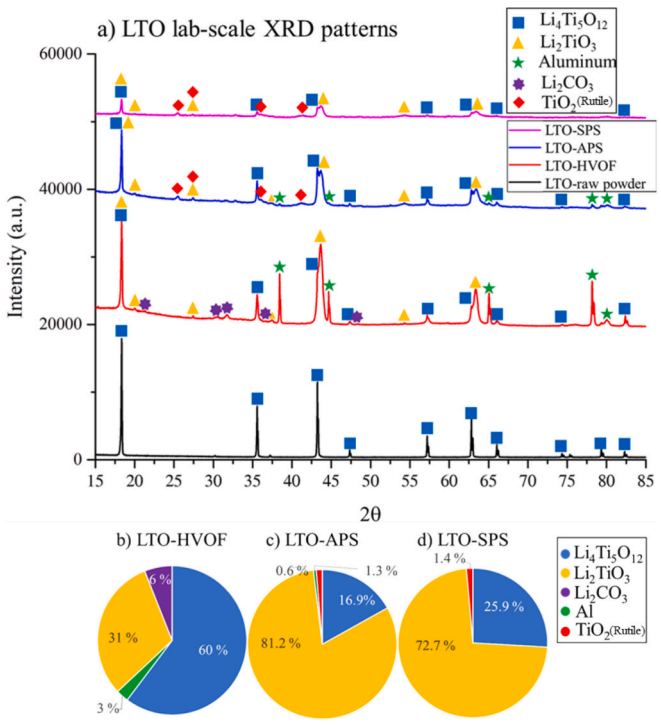

Fig. 7. Laboratory XRD patterns of LTO thin-films and feedstock. Feedstock = 100 % LTO; HVOF retains ≈60 % LTO, APS ≈16.9 %, SPS ≈25.9 %. Li_2CO_3 traces appear only in HVOF due to post-spray CO_2 uptake. Lower nominal enthalpy and faster quenching favor spinel preservation.

spinel $Li_4Ti_5O_{12}$ (LTO), monoclinic Li_2TiO_3, and minor TiO_2-rutile phases, with their relative intensities varying across deposition methods. The APS thin-film exhibits a dominant Li_2TiO_3 signature (81.2 %) with a residual LTO fraction of 16.9 %, indicating extensive transformation under high nominal plasma enthalpy. The SPS thin-film shows a mixed composition of ≈ 72.7 % Li_2TiO_3, ≈ 25.9 % LTO, and ≈ 1.4 % TiO_2, whereas the HVOF thin-film retains ≈ 60 % LTO and ≈ 31 % Li_2TiO_3 with negligible TiO_2 reflections.

Interestingly, weak Li_2CO_3 peaks are detected only in the HVOF sample. These features likely result from post-decomposition of Li_2TiO_3 by CO_2 reaction with residual surface Li_2O species when exposed to ambient air during cooling [28]. The formation follows:

$$Li_2TiO_3 + CO_2 \rightarrow Li_2CO_3 + TiO_2 \text{ [28]} \quad (2)$$

Such carbonate formation is well-known in Li-based ceramics processed under reducing or neutral environments. Since Li_2CO_3 is electronically and ionically insulating, even limited surface coverage can influence electrode kinetics, as further evidenced by the XPS analysis (Section 3.4). Additionally, the presence of weak metallic Al peaks in the APS and HVOF patterns indicates partial diffraction from the underlying substrate.

The overall trends observed by lab XRD are consistent with those from synchrotron μXRD, confirming that APS undergoes the greatest degree of phase transformation, SPS exhibits an intermediate level, while HVOF best preserves the spinel structure. Minor quantitative discrepancies between the two techniques arise from their different sampling volumes μXRD probes localized micron-scale regions, whereas lab XRD averages over the area of thin-film. Nonetheless, both datasets collectively demonstrate that higher nominal process enthalpy and longer particle exposure promote Li volatility and LTO decomposition, whereas shorter residence time and rapid quenching, as in HVOF, minimize phase instability [13].

It is important to note that lab XRD primarily probes the near-surface region, typically a few microns deep depending on thin-film density, incident beam angle, and Cu Kα wavelength (~λ = 1.54 Å). Consequently, the detected phases mainly represent surface layers, which are most affected by oxidation, cooling gradients, and post-deposition reactions. In contrast, synchrotron μXRD employs a high-flux, tightly focused beam of higher energy capable of penetrating tens of microns into the lamella, enabling through-thickness phase mapping. Hence, lab XRD may overestimate decomposition products, while μXRD offers a more representative view of the bulk composition.

Moreover, μXRD detects finer reflections from minor phases that remain unresolved in lab XRD, reflecting its higher sensitivity to minor or metastable phases. Together, these complementary techniques provide a comprehensive understanding of phase evolution from local microstructural gradients to bulk-averaged crystallography allowing precise correlation between processing conditions, thermal exposure, and LTO phase stability.

Overall, the results confirm that HVOF best retains the parent LTO phase, while APS and SPS undergo pronounced decomposition into Li_2TiO_3 and TiO_2. Maintaining a high spinel fraction is essential because secondary phases such as Li_2TiO_3 and Li_2CO_3 degrade the flat-potential behavior and cycling reversibility of LTO electrodes. Therefore, careful control of process nominal enthalpy, particle dwell time, and quenching rate is vital to preserve spinel integrity in thermally sprayed LTO films.

3.3. Depth-resolved phase distribution and interface analysis

Synchrotron-based μXRD was further employed to study depth-resolved phase distribution and interface characteristics within the thermally sprayed LTO thin-films. These analyses provide insight into micro- to meso-scale compositional gradients and reveal how the distinct thermal and chemical environments of APS, HVOF, and SPS influence local phase stability and substrate interaction.

3.3.1. Local compositional variations

In Fig. 8, the synchrotron μXRD patterns integrated over three distinct regions within the LTO-APS thin-film (highlighted by green lines) reveal the presence of multiple crystalline phases, deviating from the expected pure spinel LTO. These bright spots correspond to thermally transformed zones and provide direct evidence of the localized phase transformations also identified in the bulk analyses (Figs. 5 and 7). Each of the three regions exhibits Li_2TiO_3 and TiO_2 peaks, confirming partial decomposition of LTO in specific micro-areas of the thin-film.

At Spots 1 and 2, where the probed regions were larger, traces of unreacted LTO were also detected in addition to the transformed phases. According to Fig. 8 (e–g), the main difference among the three spots lies in the relative phase proportions: Spot 3 contains the highest amount of Li_2TiO_3 (87.4 %) and TiO_2 (12.6 %), while Spot 1 retains the largest fraction of unreacted LTO (25.4 %) together with 74.6 % Li_2TiO_3. In all analyzed locations, Li_2TiO_3 appears as the dominant phase within the localized bright areas, signifying micro-regions that experienced higher in-flight heating or longer plasma exposure.

These transformed bright spots are distributed heterogeneously across the thin-film and explain the consistent presence of Li_2TiO_3 detected in both the synchrotron and laboratory XRD analyses of LTO thin-films fabricated by HVOF, APS, and SPS. However, despite the dominance of Li_2TiO_3 within these confined areas, their overall volume fraction is limited; thus, LTO remains the primary phase when averaged over the full thin-film thickness. This observation highlights the inherent micro-scale non-uniformity typical of plasma-sprayed ceramics, where rapid thermal cycling and splat solidification produce localized transformation zones embedded within an otherwise spinel-rich matrix.

3.3.2. Top-to-bottom phase distribution

To investigate the effect of manufacturing method on the uniformity and integrity of phase distribution within the thin-film, synchrotron μXRD analysis was performed on two distinct regions (the top and bottom) of all three thin-films (HVOF, APS, and SPS). As illustrated in

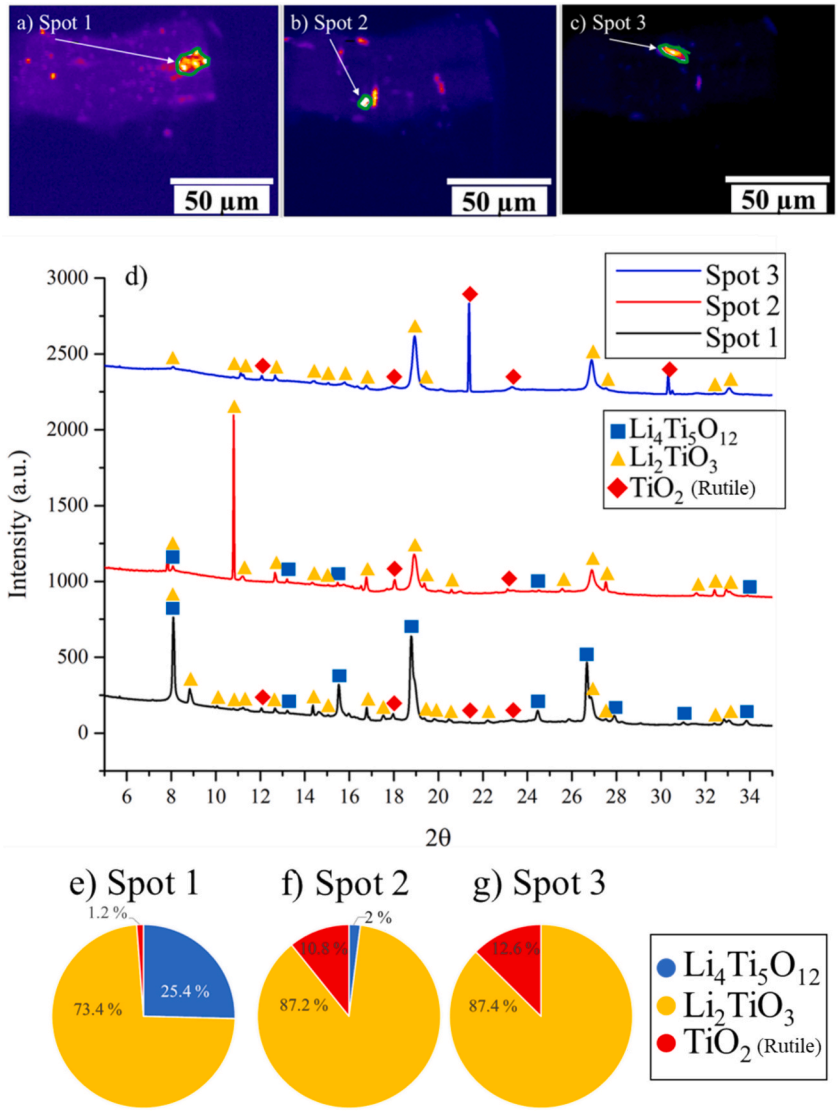

Fig. 8. a-c) Synchrotron µXRD areas integrated over three distinct regions in the LTO-APS thin-film, where in spot 1 the diffraction is corresponded to $2\theta = 7.95$, in the spot 2 the diffraction is corresponded to $2\theta = 10.73$, and in the spot 3 the diffraction is corresponded to $2\theta = 21.73$, d) Synchrotron µXRD patterns integrated over four distinct regions, e-g) phase percentages of spots 1–3 in the LTO-APS thin-film.

Fig. 9, the µXRD results reveal that in both HVOF and APS thin-films there are no significant variations in diffraction peaks, and consequently in phase composition, between the top and bottom areas. This uniformity arises mainly from the relatively thin-film thicknesses (~18 and 40 µm for HOVF and APS, respectively) and the high thermal conductivity of the aluminum substrate, which ensures efficient heat dissipation during spraying. As a result, both the upper and lower regions of these thin-films experience nearly identical cooling rates and thermal histories, yielding consistent phase composition through the thickness.

In contrast, the SPS thin-film which is sprayed onto the low-thermal-conductivity stainless-steel (SS-304) substrate exhibits a few notable differences between the top and bottom sections. These differences can be attributed to its greater thickness (~70 µm) and the slower heat conduction of the steel substrate, which allows localized overheating and delayed solidification near the interface [12]. In Fig. 9-b, c, and 9-e, f, the uniformly bright appearance without visible color contrast between the top and bottom regions indicates a homogeneous phase distribution across the entire thin-film in HVOF and APS samples. However, in Fig. 9-h and 9-i, a distinct color change appears near the substrate region (SS-304), confirming that the phase distribution differs between the top and bottom portions of the SPS thin-film.

It should also be noted that variations in peak intensity across all patterns (Fig. 9-a, d, g) originate from insufficient statistics of reflections from specific crystallographic planes within each phase caused by a limited number of grains probed by the micro beam, rather than from compositional differences. Only in Fig. 9-g, corresponding to the SPS thin-film, two distinct peaks are observed between the top and bottom patterns, providing direct evidence of a through-thickness gradient in phase constitution. This finding reinforces the conclusion that substrate thermal conductivity and thin-film thickness jointly control the spatial phase uniformity during thermal spraying.

3.3.3. *Interface behavior and substrate effects*

The synchrotron µXRD analysis presented in Fig. 10 provides a detailed view of the phase composition at the thin-film–substrate interfaces for the three processes which are aluminum substrates for HVOF and APS, and stainless steel 304 (SS-304) for SPS. Unlike conventional laboratory XRD, which operates in reflection mode and probes only the upper 5–10 µm due to limited beam penetration, synchrotron µXRD, operating in transmission mode, employs a high-intensity microbeam with superior spatial resolution, enabling localized phase identification

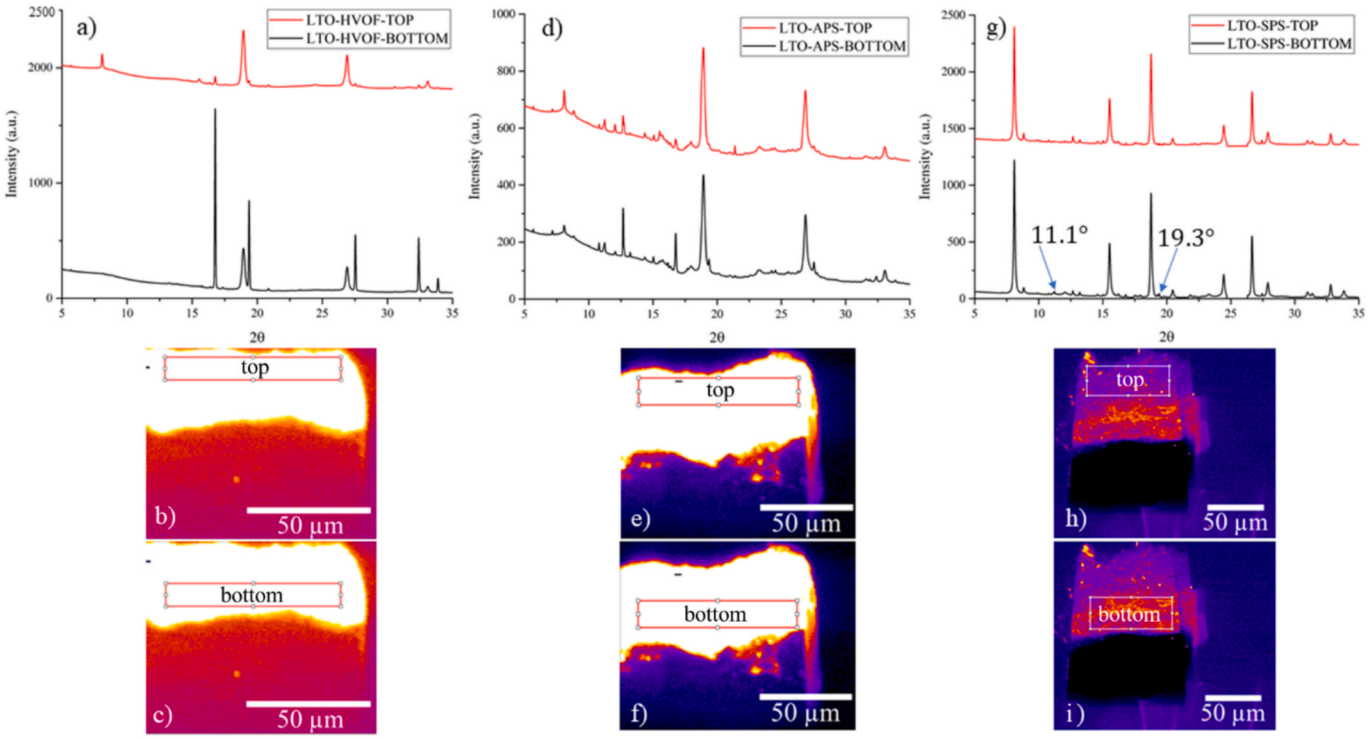

Fig. 9. Synchrotron µXRD areas generated from selected areas from top and bottom sections integrated over LTO thin-films to show the phase distribution in the top and bottom part of LTO thin-films, a, b, c) LTO-HVOF, d, e, f) LTO-APS, g, h, i) LTO-SPS.

directly at the interface. This spatially-resolved capability reveals pronounced process-dependent differences in interfacial chemistry.

For the HVOF-sprayed LTO thin-film (red pattern, Fig. 10-e), the interface exhibits dominant LTO peaks (62.3 %), moderate Li_2TiO_3 (27.1 %), and a minor Al signal (10.5 %). The well-preserved LTO fraction and weak substrate reflection indicate minimal thermal degradation and negligible interfacial reaction, consistent with HVOF's lower flame temperature and high particle velocity, which reduce dwell time at elevated temperature.

The APS-sprayed thin-film (blue pattern, Fig. 10-f) shows a more significant Li_2TiO_3 presence (49.5 %) and stronger Al substrate signal (15.3 %), with only 35.2 % LTO retained. The higher nominal plasma enthalpy and longer exposure typical of APS promote partial LTO decomposition, driving lithium volatilization and oxidation to form Li_2TiO_3.

At the SPS interface (pink pattern, Fig. 10-g), the XRD pattern is dominated by the SS-304 substrate reflections (55.1 % FCC + 6.7 % BCC), accompanied by a diminished LTO phase (36.8 %) and minor Li_2TiO_3 (6.7 %). These results indicate limited LTO crystallinity and weak thin-film retention near the interface, likely due to rapid solidification of fine suspension droplets and steep thermal gradients that hinder full crystallization or densification. The simultaneous detection of BCC and FCC phases of SS-304 confirms partial BCC → FCC transformation in the interfacial zone, attributed to the intense local heating and rapid quenching inherent to the SPS process [12].

Overall, the interface analysis underscores how substrate thermal conductivity and process nominal enthalpy govern interfacial stability. Aluminum's high thermal diffusivity ensures fast cooling, whereas stainless steel's lower conductivity prolongs heat retention, enabling phase transformations within both thin-film and substrate.

3.3.4. *Implications*

The combined findings from Figs. 8–10 establish a clear, process-dependent hierarchy of structural and chemical integrity among the thermally sprayed LTO thin-films. HVOF demonstrates the most uniform and phase-stable microstructure, maintaining a high fraction of spinel LTO and showing minimal substrate interaction due to its lower thermal load, short particle dwell time, and efficient quenching on the high-conductivity aluminum substrate. APS, by contrast, exhibits moderate compositional heterogeneity, consistent with its higher plasma temperature and longer exposure time, which promote partial LTO decomposition to Li_2TiO_3. The SPS thin-film displays the greatest structural gradient and interfacial modification, including Fe diffusion and localized BCC → FCC transformation of the stainless-steel substrate, arising from the combined effects of intense plasma–liquid interaction, droplet-based deposition, and reduced substrate thermal conductivity.

These observations collectively demonstrate that thermal history, substrate conductivity, and particle heating dynamics are the dominant parameters controlling phase evolution and interfacial chemistry in thermally sprayed LTO systems. The results also highlight that even when identical feedstock chemistry is used, the thermal–kinetic balance intrinsic to each deposition process deterministically governs lithium retention and phase stability.

From a functional perspective, maintaining a high LTO fraction and minimizing Li_2TiO_3 and TiO_2 formation are crucial for preserving the zero-strain spinel structure and its favorable electrochemical plateau behavior. Conversely, excessive Li_2TiO_3 or interfacial Li depletion can increase impedance and reduce capacity. Therefore, optimizing process nominal enthalpy and substrate heat management emerges as a direct route to enhancing both structural uniformity and electrochemical performance in plasma- and high velocity flame-sprayed battery electrodes.

Bulk XRD provided an overview of the thin-film phases, while synchrotron µXRD delivered depth-resolved insights into phase stability. However, both methods do not capture the fate of lithium at the very surface, where evaporation and environmental reactions are most evident. To address this, XPS was employed as a complementary surface-sensitive probe, enabling direct assessment of the chemical states of lithium and its interaction with the deposition environment.

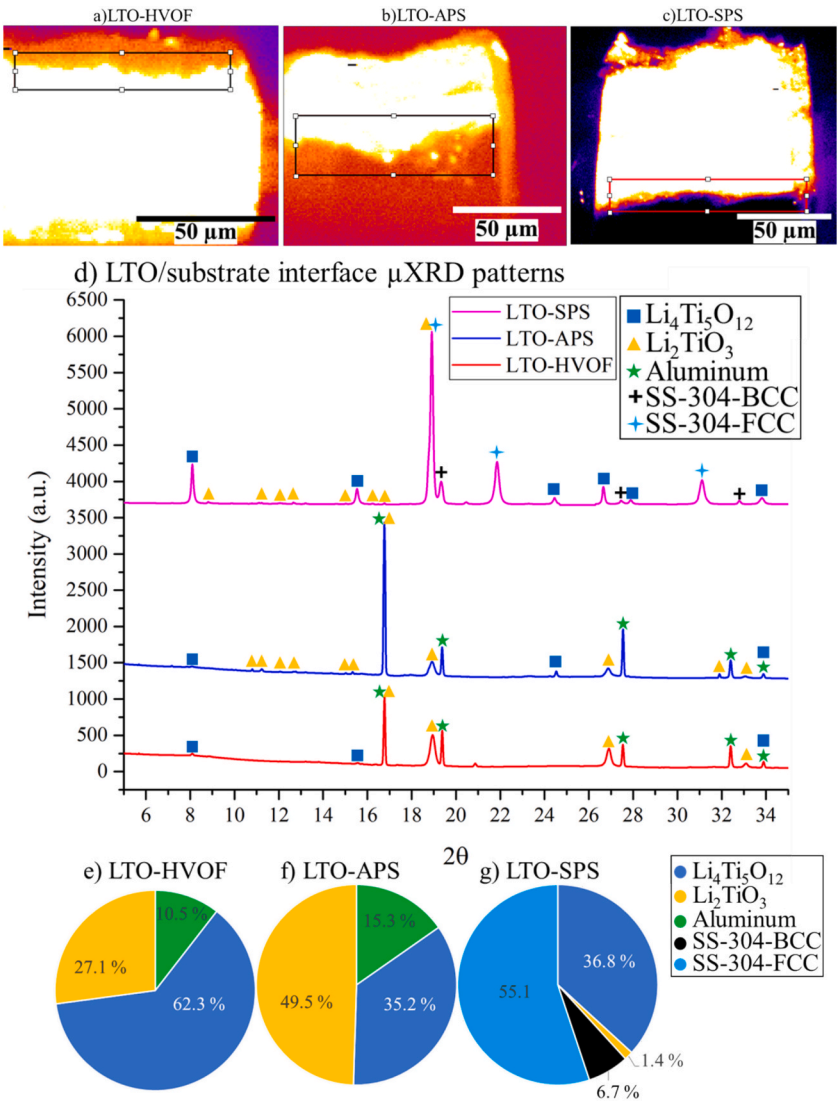

Fig. 10. Synchrotron µXRD areas integrated over LTO/substrate interfaces, a) LTO-HVOF, b) LTO-APS, c) LTO-SPS, d)Synchrotron µXRD patterns integrated over LTO/substrate interfaces, e) phase percentages at LTO-HVOF/Al substrate, f) phase percentages at LTO-APS/Al substrate, g) phase percentages at LTO-SPS/SS-304 substrate.

3.4. Surface chemistry via XPS

The XPS spectra of the three thin-films revealed distinct variations in the lithium and carbon states depending on the deposition process. The Li 1 s Lithium peaks obtained for the three processes that is in HVOF, APS and SPS are presented in Fig. 11-a-c respectively while their corresponding C 1 s carbon peaks are presented in Fig. 11-d-f. In the HVOF thin-film, the Li 1 s peak appeared at 56.5 eV (Fig. 11-a), corresponding to lithium in Li_2CO_3 form. Similarly, the APS thin-film exhibited a Li 1 s feature at a slightly lower binding energy of 56.06 eV (Fig. 11-b), also consistent with carbonate states. The higher binding energy shift in HVOF suggesting a stronger contribution from Li_2CO_3. By contrast, the SPS thin-film did not exhibit any detectable Li 1 s peak (Fig. 11-c), indicating severe lithium depletion at the outer surface of the thin-film. The C 1 s spectra further supported these observations. All thin-films contained a C-C component at ~ 284.8 eV, which is assigned to adventitious carbon and is used as charge referencing. For the HVOF thin-film, the C1s (Fig. 11-d) second peak at ~ 286.1 eV is attributed to C-O species such as alcohols or ethers, while the component at ~ 287.3 eV is assigned to C=O functional groups. Most notably, a strong feature at ~ 289.66 eV was detected, which is characteristic of carbonate ($CO3^{2-}$) species. The concurrent presence of a Li 1 s peak at 56.49 eV confirms that this carbonate is lithium carbonate (Li_2CO_3), formed by reaction of lithium species with atmospheric CO_2 during cooling. Together, these peaks indicate that in HVOF, lithium is retained at the surface and predominantly stabilizes as Li_2CO_3. In the APS thin-film, the C1s (Fig. 11-e) peak distribution was broadly similar, showing C-C at 284.8 eV, C-O at 285.98 eV, C=O at 287.6 eV, and carbonate at 289.53 eV, again consistent with Li_2CO_3. In addition, the APS spectrum showed an extra feature at ~ 291.1 eV, which is assigned to the shake-up satellite of sp^2 carbon. This signal, absent in HVOF, suggests deposition of graphitic carbon fragments in the plasma environment. In contrast, the SPS thin-film displayed a different surface chemistry. The C 1 s (Fig. 11-f) spectrum showed C-C at 284.8 eV, C-O at 286.5 eV, and a strong O-C=O peak at 288.8 eV, typically associated with organic carboxyl or ester groups. However, no carbonate peak at ~ 289.5 eV was detected, and importantly, no Li 1 s signal was observed. This indicates that the surface of SPS thin-films is lithium-depleted, likely due to lithium volatilization during spraying and reactions with water vapor from the suspension feedstock, which promote the escape of Li as volatile LiOH (g). The O-C=O peak thus reflects organic residues or environmental contamination rather than lithium carbonate. These results are

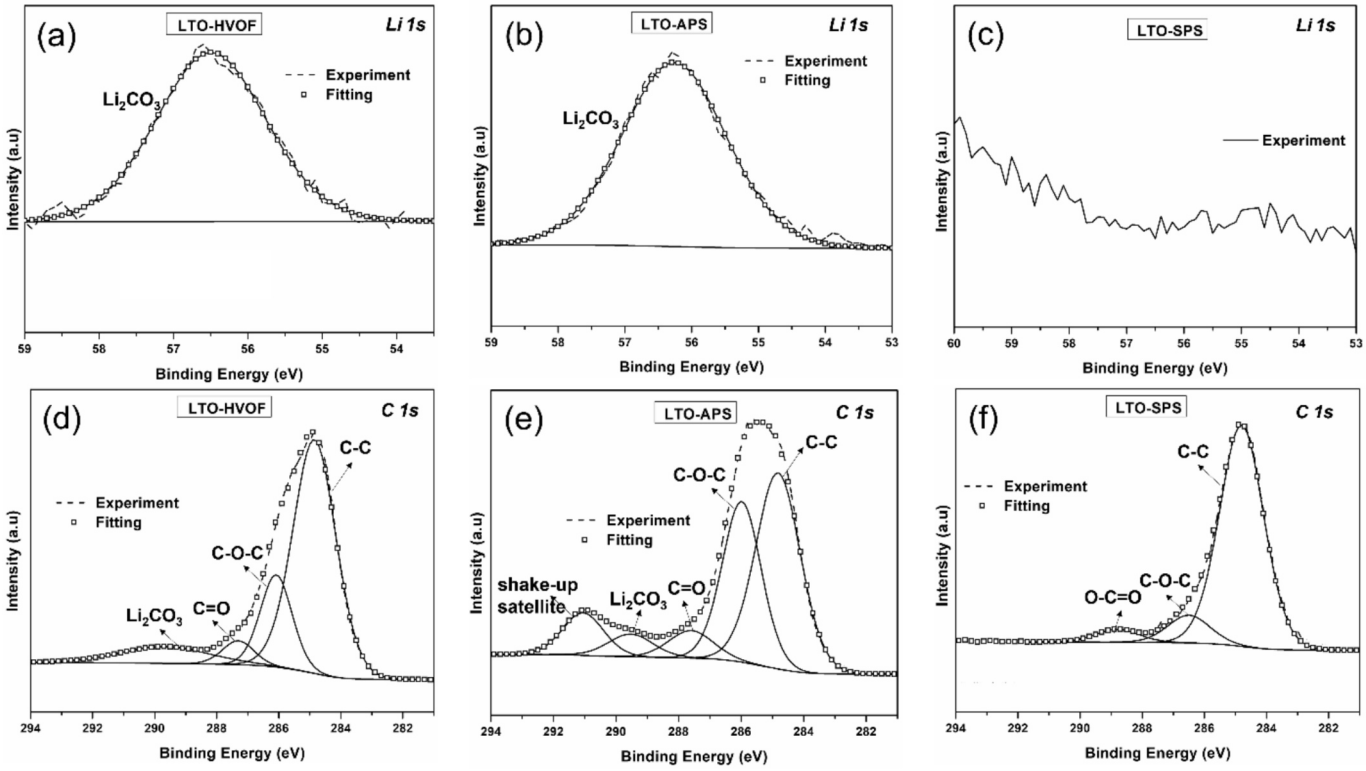

Fig. 11. XPS spectra of Li 1 s in LTO thin-films produced by (a) HVOF, (b) APS, and (c) SPS, with their corresponding C 1 s regions shown in (d-f).

summarized in Table 4.

These results demonstrate a clear process-dependent trend in surface lithium chemistry. The presence of Li 1 s and carbonate-related C 1 s peaks in APS and HVOF thin-films indicates that lithium, though partially lost during spraying, remained at the surface and reacted with atmospheric CO_2 during cooling to form Li_2CO_3 passivation layers. The slightly higher binding energy of Li 1 s in HVOF compared to APS suggests a stronger carbonate contribution in HVOF, consistent with its lower flame temperature and shorter particle residence time, which favor lithium retention. In contrast, the absence of a Li 1 s signal in the SPS thin-film points to severe surface lithium reduction, likely due to the combined effects of extreme plasma heating and water-based solvent evaporation in the suspension, which promote the evaporation of lithium as LiOH(g). It is important to emphasize that the absence of Li in the SPS surface does not mean its complete depletion from the thin-film. Both bulk XRD and synchrotron μXRD analyses confirmed the presence of lithium-titanate phases within the thin-film volume. However, as XPS is highly surface-sensitive (sampling only a few nanometers), these measurements specifically capture the final interaction of lithium with the spraying environment at the surface layer. In this regard, the XPS results complement the bulk diffraction data, revealing that while lithium remains incorporated in the thin-film, its near-surface state differs considerably across the three deposition techniques: HVOF preserved lithium most effectively, APS exhibited partial retention, and SPS showed almost complete surface depletion. This layered approach showed that how surface-sensitive techniques such as XPS provide valuable mechanistic insight into lithium-environment interactions during thermal spraying that are not accessible from bulk phase analysis alone. It must be noticed that all XPS analysis have been conducted before electrochemical testing.

3.5. *Electrochemical performance*

The cyclic voltammetry (CV) test was carried out at a scan rate of 0.1 mV/s within a 1.0–2.5 V potential range to obtain the working voltage and electrode polarization. LTO has a working voltage of 1.55 V vs Li/Li+ [59]. As shown in Fig. 12-a, a pair of reversible redox peaks was observed in the CV curves at ~ 1.5 V (i.e., oxidation voltage/ cathodic

Table 4
XPS peak-fitting results and constraints.

	SPS Binding Energy	FWHM fit parameter (eV)	Area ratio	APS Binding Energy	FWHM fit parameter (eV)	Area ratio (relative to element)	HVOF Binding Energy	FWHM fit parameter (eV)	Area ratio
C-C	284.8	1.74	1	284.8	1.75	1	284.8	1.69	1
C-O-C	286.5	1.66	0.12	285.98	1.52	0.71	286.1	1.25	0.29
C=O	–	–	–	287.6	1.75	0.14	287.3	1.25	0.08
O-C=O	288.8	1.7	0.06	–	–	–	–	–	–
Li_2CO_3 from C 1 s	–	–	–	289.53	1.75	0.12	289.66	3.5	0.15
Shakeup satellite	–	–	–	291.1	1.6	0.2	–	–	–
Li_2CO_3 from Li 1 s	–	–	–	56.06	1.91	1	56.49	1.81	1

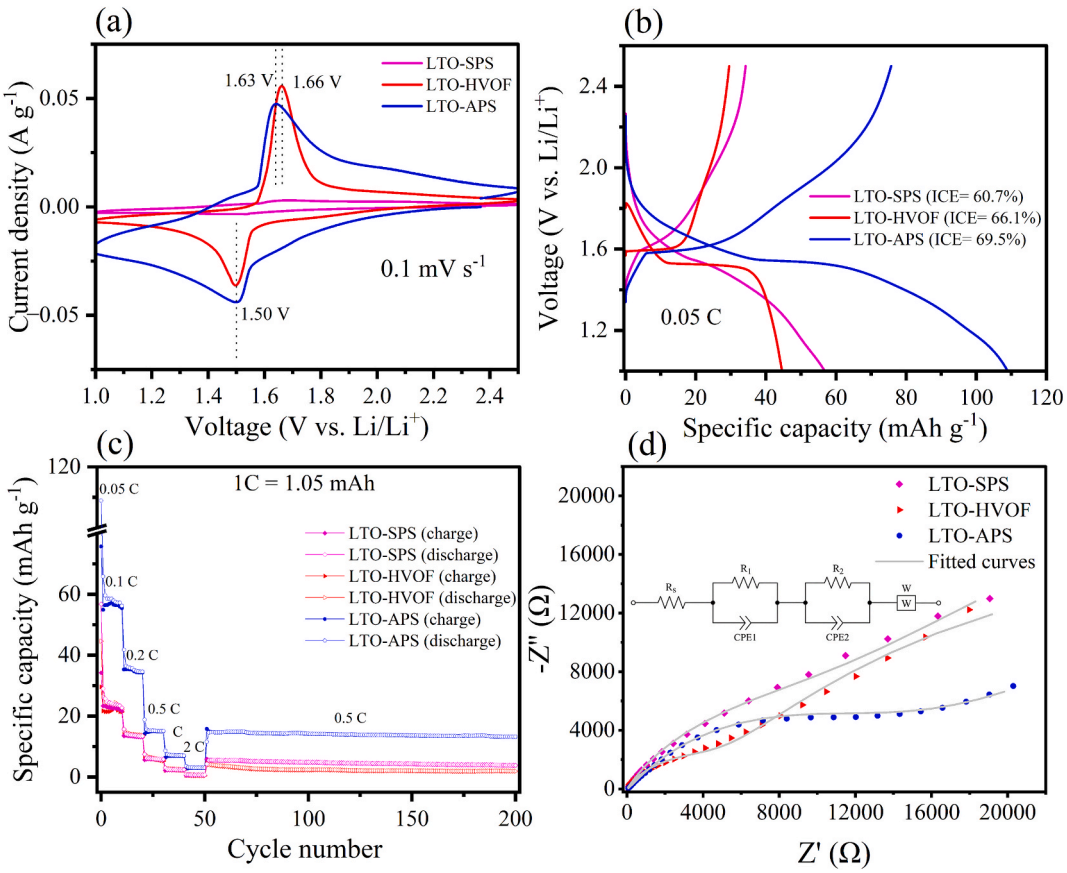

Fig. 12. a) CV curves, b) initial charge–discharge curves, c) rate and cycling performance, and d) Nyquist plot and fitted curves with corresponding equivalent circuit (inset) of LTO-HVOF, LTO-APS, and LTO-SPS anode electrodes.

potential ($E_{p,\ c}$)) for all LTO electrodes; however, in reduction voltage/potential ($E_{p,\ a}$), different values of 1.68, 1.66, and 1.63 V were observed for LTO-SPS, LTO-HVOF, and LTO-APS, respectively. These two peaks correspond to the cathodic and anodic reactions during lithiation and delithiation, respectively. From the CV curves, the working voltage (E_O) can be calculated using the equation (3) [30]:

$$E_O = \frac{E_{p,c} + E_{p,a}}{2} \tag{3}$$

The working voltage was calculated to be 1.59, 1.58, and 1.56 V for LTO-SPS, LTO-HVOF, and LTO-APS, respectively. The results show that the working voltage of LTO-APS is very close to the theoretical working voltage of LTO. The first galvanostatic charge–discharge (GCD) curves of LTO anodes at 0.05C are illustrated in Fig. 12-b. The LTO-SPS electrode doesn't show any working voltage plateaus compared to LTO-APS and LTO-HVOF, which might correspond to full decomposition of $Li_4Ti_5O_{12}$. The LTO-APS delivered the first discharge capacity of 109 mAh. g^{-1} with an initial coulombic efficiency (ICE) of 69.5 %. The LTO-SPS shows the lowest ICE of 60.7 % compared to the other LTO electrodes. The rate and cycling performance of LTO electrodes are demonstrated in Fig. 12-c. The LTO-APS showed superior rate and cycling performance after a total of 200 cycles in different C rates compared to the LTO-SPS and LTO-HVOF. Even though LTO-HVOF has a high ratio of $Li_4Ti_5O_{12}$ phase based on the XRD pattern but couldn't show promising electrochemical performance due to the existence of the 6 % Li_2CO_3 phase on the surface, which is an electronic/ionic insulator [60]. Overall, LTO-APS with the combination of $Li_4Ti_5O_{12}$ and Li_2TiO_3 without the Li_2CO_3 impurity phase showed better electrochemical performance than the other LTO electrodes.

To clarify how the coating preparation method affects interfacial reaction kinetics and Li-ion/electron transport, the LTO-SPS, LTO-HVOF, and LTO-APS electrodes were analyzed by EIS measurement. Electrochemical testing correlated the structural trends with functional performance, where APS-LTO with a voltage plateau at approximately 1.56 V vs. Li/Li+, which is consistent with the typical Ti^{4+}/Ti^{3+} redox reaction of spinel $Li_4Ti_5O_{12}$, exhibited superior cycling stability. The Nyquist plot of the electrodes and the corresponding equivalent circuit are demonstrated in Fig. 12-d. The R_s represents electrolyte and contact resistance. LTO-APS showed a resistance of 25 Ω, compared to 35 and 50 Ω for LTO-SPS and LTO-HVOF, respectively. R_1 and R_2 components contribute to the electrode/electrolyte interface, surface film formation, and charge-transfer polarization. Among the three electrodes, LTO-APS exhibited the lowest total polarization resistance ($R_{pol} = R_1 + R_2$), with a value of 18.7 kΩ, followed by LTO-SPS and LTO-HVOF, 89.3 kΩ. This lower resistance suggests that the APS electrode provides more favorable charge-transfer kinetics and more efficient Li-ion/electron transport during cycling, as can be seen in the cycling performance in Fig. 12-c. In contrast, the higher Rpol values of LTO-SPS and especially LTO-HVOF indicate stronger interfacial polarization, slower charge-transfer behavior, and more restricted transport pathways within the electrode structure. The non-ideal constant phase element (CPE) behavior, reflected by $n < 1$, suggests heterogeneous surface properties and non-uniform electrode/electrolyte contact, which was confirmed by AFM in Fig. 4. The LTO-APS with a rougher surface observed by AFM (Fig. 4) obtained a lower R_{pol}, which suggests heterogeneity of this electrode, increasing the active interfacial area rather than acting as a resistive barrier. Therefore, the coating preparation route strongly influences the Li-ion battery performance, with LTO-APS providing the most favorable kinetic response and LTO-HVOF showing the most pronounced resistive limitation.

4. Discussion

The collective structural, chemical, and electrochemical analyses converge into a unified mechanistic understanding of how process physics control phase evolution and functional response in thermally sprayed $Li_4Ti_5O_{12}$ (LTO) anodes. Each deposition method including HVOF, APS, and SPS imposes a distinct thermal–kinetic environment that determines the balance between spinel retention, lithium volatility, and interfacial stability.

(i) Thermal–kinetic control of phase evolution. The governing factor across all processes is the effective enthalpy–quench balance experienced by LTO particles or droplets. HVOF's moderate flame temperature and millisecond-scale particle flight enable rapid solidification before extensive lithium depletion, producing dense thin-films dominated by the spinel phase with only minor Li_2TiO_3. APS, with higher plasma temperature and longer residence, crosses the critical stability threshold for LTO, resulting in partial decomposition and limited lithium volatilization. SPS further amplifies these effects through plasma–liquid interaction, droplet atomization, and evaporation, generating the steepest local gradients and promoting both Li depletion and Ti-rich secondary phases.

(ii) Substrate heat conduction and interfacial chemistry. The choice of substrate governs cooling kinetics and diffusion at the thin-film base. High-conductivity aluminum (HVOF / APS) removes heat rapidly, interfacial reactions. In contrast, the low-conductivity SS-304 used for SPS sustains elevated interfacial temperatures, enabling BCC ↔ FCC transformation in steel and altering adhesion chemistry. This coupling between process nominal enthalpy and substrate diffusivity explains the observed hierarchy in interface integrity and phase uniformity. It can therefore be inferred that employing even more thermally conductive substrates such as copper or its alloys, which are also commonly used as current collectors in battery systems could further enhance interfacial stability by accelerating heat dissipation and suppressing phase degradation during deposition.

(iii) Surface chemistry and electrochemical response. Surface-sensitive XPS revealed that lithium retained in HVOF and APS thin-films reacts with atmospheric CO_2 to form thin Li_2CO_3 passivation layers, while SPS surfaces are lithium-depleted. Electrochemically, these surface phenomena directly translate into kinetic differences: carbonate films impede charge transfer in HVOF, partial carbonate and Li_2TiO_3 coexistence in APS provide the best trade-off between stability and conductivity, and Li-poor SPS thin-films display sluggish diffusion and capacity fading.

(iv) Process–structure–property paradigm: Combination of the findings from all characterization methods reveals a clear process–structure–property relationship. Among the three spraying routes, HVOF represents the low-nominal-enthalpy, high-velocity regime, whereas APS and SPS are both high-nominal-enthalpy plasma processes, although the way their thermal energy is utilized differs significantly.

In HVOF, the relatively moderate flame temperature and short dwell time allow most particles to retain the spinel LTO phase, producing a dense, uniform thin-film. A thin surface film of Li_2CO_3, formed upon air exposure, slightly limits lithium-ion transport but does not compromise stability.

In APS, the plasma torch operates at much higher nominal enthalpy, which promotes partial decomposition of LTO and formation of Li_2TiO_3. Yet, this mixture appears to provide a beneficial balance between conductivity and structural stability, resulting in the best overall electrochemical response among the three processes.

The SPS process involves even greater effective energy input but a considerable portion of that energy is consumed in solvent evaporation and droplet atomization before the submicron LTO particles are melted. For typical suspension plasma spraying (SPS) more than 50 % and up to 90 % of the thermal energy goes into solvent evaporation [61,62,63]. The use of water as the solvent further intensifies the issue: vaporization not only consumes thermal energy but can also promote lithium depletion and hydroxide-related reactions. Consequently, SPS thin-films show greater through-thickness gradients, interfacial diffusion on the stainless-steel substrate, and lower overall performance. Replacing water with less reactive organic solvents such as ethanol could potentially improve the process by reducing lithium volatility and allowing more of the plasma energy to be used for particle melting.

Finally, since substrate heat conduction strongly influences quenching and interfacial reactions, one can infer that using even more conductive substrates, such as copper or its alloys, which are commonly used as current collectors in battery systems, could further stabilize the thin-film interface by accelerating heat removal and suppressing phase degradation during deposition.

The mechanistic relationships derived from the microstructural, chemical, and electrochemical analyses are consolidated in Fig. 13, which schematically maps how variations in process nominal enthalpy, particle dynamics, and substrate heat transfer translate into distinct phase assemblages and functional responses in the thermally sprayed LTO thin-films.

5. Conclusion

The process–structure–property relationships in the thermally sprayed LTO thin-films arise from how each deposition method shapes the thermal and chemical environment experienced by the particles. Process parameters such as nominal enthalpy, particle temperature and velocity, feedstock state, and substrate thermal conductivity govern lithium volatilization, LTO decomposition, and quenching behavior, which in turn determine the resulting microstructure and phase composition. These structural outcomes, including the relative fractions of LTO, Li_2TiO_3, and TiO_2, thin-film roughness, and interfacial stability, then control the surface chemistry, such as Li_2CO_3 formation or lithium depletion. Ultimately, this combined structural and surface evolution dictates the electrochemical response. The first response indicates that thin-film with higher LTO retention and stable interfaces show better voltage behavior and cycling stability. However, the second response shows that carbonate-rich or Li-depleted surfaces exhibit reduced performance. In essence, the process sets the thermal–chemical conditions, which determine the structure, which then dictates the properties.

This study establishes a comprehensive understanding of how different thermal spray processes including HVOF, APS, and SPS govern phase changes, interfacial chemistry, and electrochemical behavior in $Li_4Ti_5O_{12}$ (LTO) thin-films. Synchrotron and laboratory XRD analyses confirmed that all thin-films contained the spinel LTO phase along with Li_2TiO_3 and minor presence of TiO_2, yet their relative fractions varied distinctly with processing conditions. HVOF retained the highest proportion of spinel, APS showed moderate transformation, while SPS experienced the most severe decomposition, highlighting the role of process nominal enthalpy and dwell time in lithium volatility and phase stability because of water solvent and finer particle size.

Spatially-resolved μXRD revealed uniform phase distributions in thin-films produced on aluminum substrates (HVOF and APS) but strong through-thickness gradients and interfacial diffusion in SPS on SS-304. The interfacial analysis indicated limited substrate involvement in HVOF and APS, in contrast to SPS, where Fe diffusion and partial BCC → FCC transformation occurred at the thin-film base. XPS confirmed surface Li_2CO_3 formation on APS and HVOF thin-films due to ambient carbonation, whereas SPS surfaces were lithium-depleted, evidencing the combined effects of feedstock state and plasma–liquid interaction on surface chemistry.

These structural and chemical trends were directly reflected in electrochemical performance. APS thin-films, with a mixed LTO–Li_2TiO_3 composition, exhibited the most favorable combination of capacity and stability. HVOF thin-films were structurally robust but kinetically limited due to carbonate films, while SPS thin-films suffered from lithium depletion and compositional gradients, resulting in inferior performance.

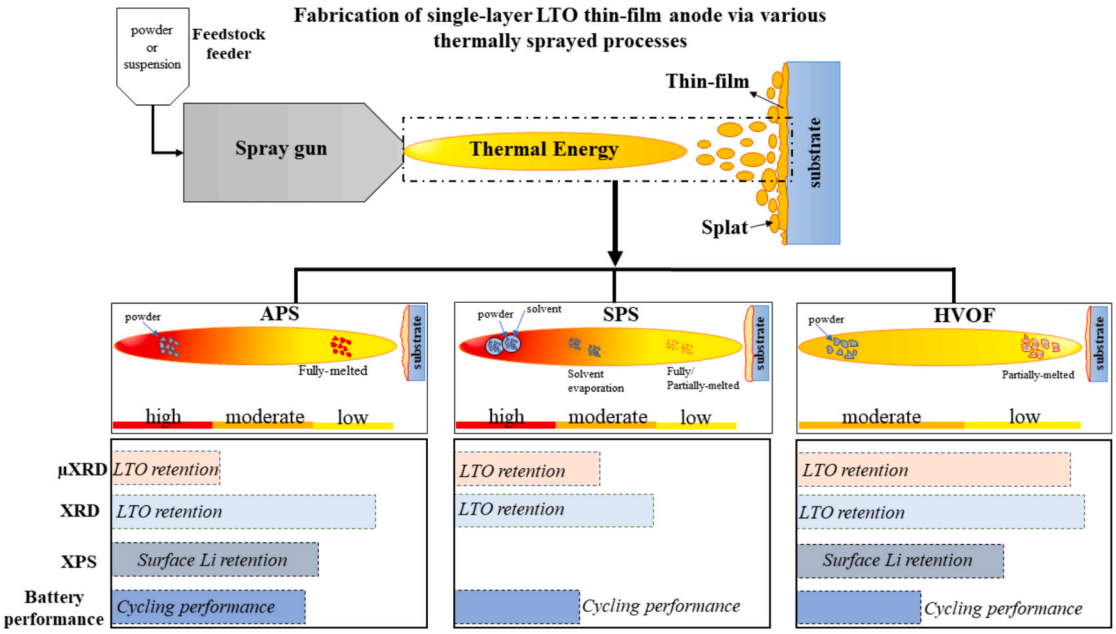

Fig. 13. Schematic overview of processing–structure–property relationships in thermally sprayed LTO thin films.

The integrated process–structure–property framework developed here demonstrates that the enthalpy–quench balance, substrate conductivity, and solvent chemistry jointly determine phase stability and interfacial integrity. Using more thermally conductive current collectors, such as copper or its alloys, could further improve interface quality, while adopting less reactive solvents like ethanol in SPS may enhance energy utilization and lithium retention. This work provides a mechanistic foundation for designing next-generation thermally sprayed oxide electrodes. Process energy, substrate selection, and feedstock formulation can be precisely tuned to achieve stable, high-performance large-area thin-films for solid-state and thin-film battery applications.

CRediT authorship contribution statement

Arman Hasani: Writing – review & editing, Writing – original draft, Validation, Software, Methodology, Formal analysis, Data curation, Conceptualization. **Antti Salminen:** Writing – review & editing, Supervision, Resources, Project administration, Funding acquisition, Conceptualization. **Shrikant Joshi:** Writing – review & editing, Resources, Project administration, Methodology, Investigation, Funding acquisition, Conceptualization. **Malgorzata Grazyna Makowska:** Writing – review & editing, Validation, Supervision, Software, Project administration, Methodology, Investigation, Data curation, Conceptualization. **Behnam Chameh:** Writing – review & editing, Writing – original draft, Methodology, Investigation, Formal analysis. **Vesa-Pekka Lehto:** Writing – review & editing, Methodology, Conceptualization. **Vinay Gidla:** Writing – review & editing, Writing – original draft, Methodology, Investigation, Formal analysis, Conceptualization. **Sneha Goel:** Writing – review & editing, Supervision, Funding acquisition, Conceptualization. **Ilari Angervo:** Writing – review & editing, Methodology. **Ashish Ganvir:** Writing – review & editing, Writing – original draft, Validation, Supervision, Resources, Project administration, Methodology, Investigation, Funding acquisition, Conceptualization.

Funding

This research was supported by the GREEN-BAT project (2022–2025) under the M-ERA.Net framework. The authors acknowledge funding from the Research Council of Finland, M-ERA.NET 3 through the European Commission, and the national and regional financiers in Germany and Sweden. Prof. Ashish Ganvir acknowledges the SOLACE (DNR 360540) Academy research fellowship, funded by the Research Council of Finland and also extends his gratitude to the City of Turku for supporting his tenure-track grant. The work in Sweden, carried out at University West, received additional support from the NovelCABs proof-of-concept project, funded by the Swedish Energy Agency (Energimyndigheten, Dnr 2021-002227), and from Vinnova, the Swedish Governmental Agency for Innovation Systems, within the M-ERA.NET 3 GREEN-BAT initiative. This project has also received funding from the European Union's Horizon 2020 research and innovation programme under grant agreement No 958174.The authors also acknowledge the Finnish Digital Design and Manufacturing Infrastructure (FiDiEm) infrastructure for access to the experimental facilities.

Declaration of competing interest

The authors declare that they have no known competing financial interests or personal relationships that could have appeared to influence the work reported in this paper.

Acknowledgement

The authors gratefully acknowledge Stefan Björklund from University West, Trollhättan, Sweden, for his expertise in plasma spraying of battery materials and for conducting electron microscopy characterizations, as well as Aki Piiroinen from the University of Turku for his support with surface roughness testing. The author gratefully acknowledges Sandra Johansson Storm and Killian Clovis from University West, Trollhättan, Sweden, for their support and for providing valuable information and materials that contributed to this work. The authors also wish to thank the Swiss Light Source (SLS) in Paul-Scherrer Institute (PSI) for providing beamtime at the microXAS beamline, and Joakim Reuteler at ETH Zurich for providing Focused Ion Beam milling facilities.

Declaration of generative AI and AI-assisted technologies in the manuscript preparation process

During the preparation of this work the author(s) used [ChatGPT] in order to [English Language Proofreading]. After using this tool/service, the author(s) reviewed and edited the content as needed and take(s) full

responsibility for the content of the published article.

Data availability

Data will be made available on request.

References

[1] I.T. Adebanjo, et al., A comprehensive review of lithium-ion battery components degradation and operational considerations: a safety perspective, Energy Adv. 4 (7) (2025) 820–877, https://doi.org/10.1039/D5YA00065C.

[2] C.M. Julien, A. Mauger, Fabrication of Li4Ti5O12 (LTO) as Anode Material for Li-Ion Batteries, Micromachines (Basel) 15 (3) (2024) 310, https://doi.org/10.3390/mi15030310.

[3] A. Ghosh, F. Ghamouss, Role of Electrolytes in the Stability and Safety of Lithium Titanate-based Batteries, Front. Mater. 7 (2020), https://doi.org/10.3389/fmats.2020.00186.

[4] L. Su, M.Z. Bazant, A. Millner, P. Bai, Degradation of commercial Li4Ti5O12-based lithium-ion batteries under extremely fast cycling rates, Appl. Energy 386 (2025) 125594, https://doi.org/10.1016/j.apenergy.2025.125594.

[5] Y. Chen, et al., Nonequilibrium fast-lithiation of Li4Ti5O12 thin film anode for LIBs, Commun. Phys. 7 (1) (2024) 280, https://doi.org/10.1038/s42005-024-01775-7.

[6] J. Speulmanns, S. Bönhardt, W. Weinreich, and P. Adelhelm, "Interface-Engineered Atomic Layer Deposition of 3D Li4Ti5O12 for High-Capacity Lithium-Ion 3D Thin-Film Batteries," Apr. 19, 2024. doi: 10.26434/chemrxiv-2024-qhtkh.

[7] Z. He, et al., Conductive surface modification with copper of Li4Ti5O12 as anode materials for Li-ion batteries, Mater. Lett. 107 (2013) 273–275, https://doi.org/10.1016/j.matlet.2013.06.025.

[8] M. Gockeln, et al., Enhancing the utilization of Porous Li $_4$ Ti $_5$ O $_{12}$ Layers for Thin-Film Lithium-Ion Batteries, ACS Appl. Energy Mater. 3 (10) (2020) 9667–9675, https://doi.org/10.1021/acsaem.0c01231.

[9] W. Wang, B. Jiang, W. Xiong, Z. Wang, S. Jiao, A nanoparticle Mg-doped Li4Ti5O12 for high rate lithium-ion batteries, Electrochim. Acta 114 (2013) 198–204, https://doi.org/10.1016/j.electacta.2013.10.035.

[10] B. Gangaja, S. Nair, D. Santhanagopalan, Surface-Engineered Li4Ti5O12 Nanostructures for High-Power Li-Ion Batteries, Nanomicro Lett. 12 (1) (2020) 30, https://doi.org/10.1007/s40820-020-0366-x.

[11] K. Su, C. Tang, C. Li, S. Weng, Y. Xiang, X. Peng, Yttrium-doped Li4Ti5O12 nanoparticles as anode for high-rate and high-energy lithium-ion batteries, Discover Nano 19 (1) (2024) 213, https://doi.org/10.1186/s11671-024-04177-4.

[12] A. Hasani, et al., Localized phase and Elemental Mapping in Solid-State Lithium Battery LTO Anode Thin-Film Produced by a Novel Suspension Plasma Spray Approach, J. Therm. Spray Technol. 34 (5) (2025) 1589–1597, https://doi.org/10.1007/s11666-025-02003-6.

[13] D. Yost, J. Laurer, K. Childrey, C. Cai, G.M. Koenig, Fabrication and Characterization of Plasma Sprayed TiO2 and Li4Ti5O12 Materials as all active Material Lithium-Ion Battery Electrodes, Batteries 9 (12) (2023) 598, https://doi.org/10.3390/batteries9120598.

[14] N. Umirov, Y. Yamada, H. Munakata, S.-S. Kim, K. Kanamura, Analysis of intrinsic properties of Li4Ti5O12 using single-particle technique, J. Electroanal. Chem. 855 (2019) 113514, https://doi.org/10.1016/j.jelechem.2019.113514.

[15] S. Zhou, et al., Printed Solid-State Batteries, Electrochem. Energy Rev. 6 (1) (2023) 34, https://doi.org/10.1007/s41918-023-00200-x.

[16] F. Chen, Z.-L. Xu, Design and manufacture of high-performance microbatteries: lithium and beyond, Microstructures 2 (3) (2022) 12, https://doi.org/10.20517/microstructures.2022.10.

[17] P. Zhu, P.R. Slater, E. Kendrick, Insights into architecture, design and manufacture of electrodes for lithium-ion batteries, Mater. Des. 223 (Nov. 2022) 111208, https://doi.org/10.1016/j.matdes.2022.111208.

[18] D. Tejero-Martin, M. Rezvani Rad, A. McDonald, and T. Hussain, "Beyond Traditional Coatings: A Review on Thermal-Sprayed Functional and Smart Coatings," *Journal of Thermal Spray Technology*, vol. 28, no. 4, pp. 598–644, Apr. 2019, doi: 10.1007/s11666-019-00857-1.

[19] H. Memon, A. Rincón Romero, K. Derelizade, F. Venturi, and T. Hussain, "A new hybrid suspension and solution precursor thermal spray for wear-resistant silicon carbide composite coatings," *Mater. Des.*, vol. 224, p. 111382, 2022, doi: 10.1016/j.matdes.2022.111382.

[20] G.-S. Ham, K.-W. Kim, G.-S. Cho, C.P. Kim, K.-A. Lee, Fabrication, microstructure and wear properties of novel Fe-Mo-Cr-C-B metallic glass coating layers manufactured by various thermal spray processes, Mater. Des. 195 (2020) 109043, https://doi.org/10.1016/j.matdes.2020.109043.

[21] A. Hasani, et al., Laser Processing of Liquid Feedstock Plasma-Sprayed Lithium Titanium Oxide Solid-State-Battery Electrode, Coatings 14 (2) (2024) 224, https://doi.org/10.3390/coatings14020224.

[22] A. Hasani, et al., Advanced synchrotron micro characterization of laser post-processed plasma sprayed LLZO solid-state battery electrolyte, IOP Conf. Ser.: Mater. Sci. Eng. 1332 (1) (2025) 012022, https://doi.org/10.1088/1757-899X/1332/1/012022.

[23] V. Gopal, et al., Exploring atmospheric plasma spraying as a pathway to fabricate solid-state battery constituents, Surf. Coat. Technol. 502 (2025) 131945, https://doi.org/10.1016/j.surfcoat.2025.131945.

[24] A. Vardelle, C. Moreau, N.J. Themelis, C. Chazelas, A Perspective on Plasma Spray Technology, Plasma Chem. Plasma Process. 35 (3) (2015) 491–509, https://doi.org/10.1007/s11090-014-9600-y.

[25] M. F. SMITH, "Comparing cold spray with thermal spray coating technologies," in The Cold Spray Materials Deposition Process, Elsevier, 2007, pp. 43–61. doi: 10.1533/9781845693787.1.43.

[26] M. Oksa, E. Turunen, T. Suhonen, T. Varis, S.-P. Hannula, Optimization and Characterization of High Velocity Oxy-fuel Sprayed Coatings: Techniques, Materials, and applications, Coatings 1 (1) (2011) 17–52, https://doi.org/10.3390/coatings1010017.

[27] O. Ali, et al., Influence of Feedstock and thermal Spray Process on the phase Composition of Alumina Coatings and their Sliding Wear, J. Therm. Spray Technol. 32 (7) (2023) 2028–2053, https://doi.org/10.1007/s11666-023-01597-z.

[28] A. Kozlova, N. Uvarov, M. Sharafutdinov, E. Gerasimov, Y. Mateyshina, In situ study of solid-state synthesis of Li4Ti5O12–Li2TiO3 and Li4Ti5O12–TiO2 composites, J. Solid State Chem. 313 (2022) 123302, https://doi.org/10.1016/j.jssc.2022.123302.

[29] Y. Kang, Y. Xie, F. Su, K. Dai, M. Shui, J. Shu, α-Li $_2$ TiO $_3$: a new ultrastable anode material for lithium-ion batterie, Dalton Trans. 51 (47) (2022) 18277–18283, https://doi.org/10.1039/D2DT03115A.

[30] B. Priyono, P. B. Murti, A. Z. Syahrial, and A. Subhan, "Optimizing the performance of Li4Ti5O12 anode synthesized from TiO2 xerogel and LiOH with hydrothermal-ball mill method by using acetylene black," 2017, p. 020005. doi: 10.1063/1.4979221.

[31] B. Putz, et al., Glass and nanocrystalline phase formation in CuZrAg alloys: Insights from combinatorial thin film libraries studied by mapping synchrotron X-ray diffraction, Mater. Des. 244 (2024) 113144, https://doi.org/10.1016/j.matdes.2024.113144.

[32] C. Ioannidou, et al., In-situ synchrotron X-ray analysis of metal Additive Manufacturing: current state, opportunities and challenges, Mater. Des. 219 (2022) 110790, https://doi.org/10.1016/j.matdes.2022.110790.

[33] C. Nayak, et al., High-Resolution Synchrotron μXRD and μXRF for local phase and Elemental Analysis in Suspension Plasma Sprayed Environmental Barrier Coatings, J. Therm. Spray Technol. 35 (2–3) (2026) 650–662, https://doi.org/10.1007/s11666-026-02159-9.

[34] A. Hasani, et al., Laser post-processing as a surface engineering strategy for atmospheric plasma-sprayed thin-film all-solid-state battery components, Appl. Surf. Sci. 735 (2026) 166624, https://doi.org/10.1016/j.apsusc.2026.166624.

[35] X. Liang, Y. Wang, X. Zhang, D. Han, L. Lan, Y. Zhang, Performance study of a Li4Ti5O12 electrode for lithium batteries prepared by atmospheric plasma spraying, Ceram. Int. 45 (17) (2019) 23750–23755, https://doi.org/10.1016/j.ceramint.2019.08.091.

[36] S. Mathiyalagan, et al., Facile one-step fabrication of Li4Ti5O12 coatings by suspension plasma spraying, Mater. Res. Bull. 181 (2025) 113111, https://doi.org/10.1016/j.materresbull.2024.113111.

[37] Killian Clovis, "Deposition and characteristics of ther-mal sprayed layers as solid-state thin film battery components," University West, Trollhättan, SWEDEN, 2023.

[38] C.N. Borca, et al., The microXAS beamline at the swiss light source: Towards nano-scale imaging, J. Phys. Conf. Ser. 186 (2009) 012003, https://doi.org/10.1088/1742-6596/186/1/012003.

[39] S. Grimm, "https://www.dectris.com/en/detectors/x-ray-detectors/eiger2/eiger2-for-synchrotrons/.".

[40] A. W. Colldeweih, M. G. Makowska, O. Tabai, D. F. Sanchez, and J. Bertsch, "Zirconium hydride phase mapping in Zircaloy-2 cladding after delayed hydride cracking," *Materialia (Oxf).*, vol. 27, p. 101689, Mar. 2023, doi: 10.1016/j.mtla.2023.101689.

[41] G. Ashiotis, et al., The fast azimuthal integration Python library: *pyFAI*, J. Appl. Crystallogr. 48 (2) (2015) 510–519, https://doi.org/10.1107/S1600576715004306.

[42] V.A. Solé, E. Papillon, M. Cotte, Ph. Walter, J. Susini, A multiplatform code for the analysis of energy-dispersive X-ray fluorescence spectra, Spectrochim. Acta Part B at. Spectrosc. 62 (1) (2007) 63–68, https://doi.org/10.1016/j.sab.2006.12.002.

[43] K. Bobzin, L. Zhao, H. Heinemann, E. Burbaum, Influence of the atmospheric plasma spraying parameters on the coating structure and the deposition efficiency of silicon powder, Int. J. Adv. Manuf. Technol. 123 (1–2) (2022) 35–47, https://doi.org/10.1007/s00170-022-10008-6.

[44] M. Michalak, et al., Wear Behavior Analysis of Al2O3 Coatings Manufactured by APS and HVOF Spraying Processes using Powder and Suspension Feedstocks, Coatings 11 (8) (2021) 879, https://doi.org/10.3390/coatings11080879.

[45] N. Curry, K. VanEvery, T. Snyder, J. Susnjar, S. Bjorklund, Performance Testing of Suspension Plasma Sprayed thermal Barrier Coatings Produced with Varied Suspension Parameters, Coatings 5 (3) (2015) 338–356, https://doi.org/10.3390/coatings5030338.

[46] G. Mittal, S. Paul, Suspension and solution Precursor Plasma and HVOF Spray: a Review, J. Therm. Spray Technol. 31 (5) (2022) 1443–1475, https://doi.org/10.1007/s11666-022-01360-w.

[47] A. Ganvir, R.F. Calinas, N. Markocsan, N. Curry, S. Joshi, Experimental visualization of microstructure evolution during suspension plasma spraying of thermal barrier coatings, J. Eur. Ceram. Soc. 39 (2–3) (2019) 470–481, https://doi.org/10.1016/j.jeurceramsoc.2018.09.023.

[48] M. Bellippady, et al., Performance of Atmospheric Plasma-Sprayed thermal Barrier Coatings on Additively Manufactured Super Alloy Substrates, Coatings 14 (5) (2024) 626, https://doi.org/10.3390/coatings14050626.

[49] M.F. Bonilauri, et al., Deposition of high-velocity oxygen-fuel (HVOF) coatings on laser-powder bed fused (L-PBF) parts subjected to in-situ laser remelting

treatments, Surf. Coat. Technol. 510 (2025) 132250, https://doi.org/10.1016/j.surfcoat.2025.132250.
[50] M. Górnik, E. Jonda, M. Nowakowska, L. Łatka, The effect of Spray Distance on Porosity, Surface Roughness and Microhardness of WC-10Co-4Cr Coatings Deposited by HVOF, Adv. Mater. Sci. 21 (4) (2021) 99–111, https://doi.org/10.2478/adms-2021-0028.
[51] P. Kou, et al., Zinc-substituted Li4Ti5O12 as a novel large-capacity and low-voltage titanium-based anode material for Li-ion batteries, Mater Charact 220 (2025) 114684, https://doi.org/10.1016/j.matchar.2024.114684.
[52] J.P. Pender, et al., Electrode Degradation in Lithium-Ion Batteries, ACS Nano 14 (2) (2020) 1243–1295, https://doi.org/10.1021/acsnano.9b04365.
[53] A. Watanabe, et al., Structural analysis of imperfect Li2TiO3 crystals, J. Alloys Compd. 819 (2020) 153037, https://doi.org/10.1016/j.jallcom.2019.153037.
[54] B. Xu, D. Qian, Z. Wang, Y.S. Meng, Recent progress in cathode materials research for advanced lithium ion batteries, Materials Science and Engineering: R: Reports 73 (5–6) (2012) 51–65, https://doi.org/10.1016/j.mser.2012.05.003.
[55] Carmen. de la Torre-Gamarra *et al.*, "Tape casting manufacturing of thick Li4Ti5O12 ceramic electrodes with high areal capacity for lithium-ion batteries," *J. Eur. Ceram. Soc.*, vol. 41, no. 1, pp. 1025–1032, 2021, doi: 10.1016/j.jeurceramsoc.2020.07.049.
[56] C. Schneider, M.G. Makowska, J. Bertsch, 3D microscopic X-ray fluorescence and diffraction analysis of a fuel-cladding interface of a highly irradiated boiling water reactor fuel rod, J. Nucl. Mater. 616 (2025) 156020, https://doi.org/10.1016/j.jnucmat.2025.156020.
[57] K. Tsuji, J. Injuk, and R. Van Grieken, Eds., *X-Ray Spectrometry: Recent Technological Advances*. Wiley, 2004. doi: 10.1002/0470020431.
[58] A. Sharma, D. Hesterberg, "Synchrotron radiation-based spatial methods in environmental biogeochemistry," in Multidimensional Analytical Techniques in Environmental Research, Elsevier, 2020, pp. 231–265. doi: 10.1016/B978-0-12-818896-5.00009-0.
[59] J.-H. Choi, et al., Multi-layer electrode with nano-Li4Ti5O12 aggregates sandwiched between carbon nanotube and graphene networks for high power Li-ion batteries, Sci. Rep. 4 (1) (2014) 7334, https://doi.org/10.1038/srep07334.
[60] L. Bläubaum, P. Röse, F. Baakes, and U. Krewer, "Impact of Lithium-Ion Battery Separators on Gas Evolution during Temperature Abuse," *Batter. Supercaps*, vol. 7, no. 3, Mar. 2024, doi: 10.1002/batt.202300534.
[61] A. Farrokhpanah, T.W. Coyle, J. Mostaghimi, Numerical Study of Suspension Plasma Spraying, J. Therm. Spray Technol. 26 (1–2) (2017) 12–36, https://doi.org/10.1007/s11666-016-0502-9.
[62] M. Jadidi, A. Vardelle, A. Dolatabadi, and C. Moreau, "Heat Transfer in Suspension Plasma Spraying," in Handbook of Thermal Science and Engineering, Cham: Springer International Publishing, 2018, pp. 2923–2966. doi: 10.1007/978-3-319-26695-4_30.
[63] E.H. Jordan, C. Jiang, M. Gell, The solution Precursor Plasma Spray (SPPS) Process: a Review with Energy Considerations, J. Therm. Spray Technol. 24 (7) (2015) 1153–1165, https://doi.org/10.1007/s11666-015-0272-9.